DEUTSCHES ELEKTRONEN-SYNCHROTRON
INSTITUT FÜR HOCHENERGIEPHYSIK

DESY 93–124
August 1993

Structure Functions and Parton Distributions in Deep Inelastic Lepton-Hadron Scattering at High Energies

J. Blümlein
DESY-Institut für Hochenergiephysik, Zeuthen

ISSN 0418-9833

PLATANENALLEE 6 - 15738 ZEUTHEN

To be sure that your preprints are promptly included in the
HIGH ENERGY PHYSICS INDEX,
send them to (if possible by air mail):

DESY
Bibliothek
Notkestraße 85
22603 Hamburg
Germany

DESY-IfH
Bibliothek
Platanenallee 6
15738 Zeuthen
Germany

DESY 93-124
August 1993

ISSN 0418-9833

Structure Functions and Parton Distributions in Deep Inelastic Lepton–Hadron Scattering at High Energies[1]

Johannes Blümlein

DESY – Institut für Hochenergiephysik,
Platanenallee 6, D–15735 Zeuthen, FRG

Abstract

The possibilities to measure structure functions, to extract parton distributions, and to measure α_s and Λ_{QCD} in current and future high energy deep inelastic scattering experiments are reviewed. A comparison is given for experiments at HERA, an ep option at LEP $\otimes$ LHC, and a high energy neutrino experiment.

[1] Invited Lecture at the 1993 St. Petersburg Winter School on Theoretical High Energy Physics, Gatchina, Russia, January 25 – February 5, 1993, to appear in: 'Surveys on Theoretical Physics', Gordon & Breach, Brussels, 1993.

Contents

1 Introduction

During the last 20 years deep inelastic lepton–hadron scattering has revealed a detailed picture of the nucleon structure at short distances. The discovery of the parton structure of hadrons [1] was followed by detailed studies of the flavour structure of nucleons using both neutrinos and charged lepton probes [2]. The concise measurement of the nucleon structure functions allowed precise tests of the validity of QCD predictions on their Q^2 behaviour, the extraction of the gluon distribution, and the measurement of α_s and Λ_{QCD}. So far, the kinematical range of $x \gtrsim 10^{-2}$ and $Q^2 \lesssim 200\,\mathrm{GeV}^2$ has been investigated. With the advent of HERA this range is extended to $x \gtrsim 10^{-4}$ and $Q^2 \lesssim 20.000\,\mathrm{GeV}^2$ allowing to probe the proton structure at even much shorter distances and in the *novel* range of extremely small x values. At future facilities, e.g. a combination of LEP and LHC beams, this kinematical range may be extended even further using electrons as a probe of the proton structure. As will be shown subsequently also neutrino experiments at higher energies than currently available are required complementary to $e^{\pm}N$ scattering. This is due to the observation that charged current interactions allow to disentangle the flavour structure much better than possible in neutral current reactions. At $e^{\pm}p$ facilities only a comparably small amount of charged current data is taken.

The study of deep inelastic lepton–hadron scattering in present and future $e^{\pm}N$ and νN experiments aims on high precision measurements of the individual parton distributions. These distributions serve as an input for all cross section calculations for future high energy hadron colliders. Therefore, their knowledge both at small x and high Q^2 is indispensible for the physics analysis at hadron colliders. Because a large contribution to most of these cross sections is caused by gluon–gluon fusion it is particularly important to determine the gluon distribution with high precision.

Furthermore, opening up new kinematical ranges one may search for new structures in the range of high Q^2. At small x new effects ruling the evolution of structure functions are expected. Since the statistics in this range is very high these structures can be searched for with very precise measurements. The scaling violations of the measured structure functions can be compared with the QCD predictions leading to a measurement of Λ_{QCD} and $\alpha_s(Q^2)$ in new kinematical domains.

In this lecture the prospects to investigate the nucleon structure for current and possible future $e^{\pm}N$ and νN experiments are reviewed. After a discussion of the basic scattering cross sections (section 2) the accessible kinematical ranges, expected luminosities and eventrates at HERA, LEP $\otimes$ LHC and a neutrino experiment in the TeV range are compared. The extraction of structure functions requires the knowledge of the QED radiative corrections (section 4), which were calculated for a variety of kinematical conditions. Different ways to measure single hadronic structure functions are discussed in section 5 using charged lepton and neutrino beams at proton and deuteron targets. In section 6 the prospects to unfold individual quark distributions are considered and a summary on the status of parton–parametrizations is given. The knowledge of the gluon distribution is of special importance for future experiments at hadron colliders like SSC or LHC. The extraction of this distribution is particularly difficult in deep inelastic scattering since the gauge bosons $\gamma, W^{\pm}$ and Z do not couple to gluons directly. Thus the derivation of this density requires to combine different measurements as the scaling violations of nucleon structure functions, the longitudinal structure functions, and the hard cross sections of heavy flavour and J/ψ production. This is discussed in section 7. Section 8 deals with the QCD analysis of different structure functions. Possibilities are discussed for a precise measurement of α_s in the new kinematical ranges. These estimates are compared with measurements of α_s in other hard processes. The experimental access to the new kinematical range $x \lesssim 10^{-2}$ will

allow to test the validity of QCD also in the semi–hard range. Particularly, a lowering in the rise of the structure functions due to higher twist effects as compared with the Altarelli–Parisi evolution could be one signature to be observed. Ways to extract this effect are discussed in section 9. The first results from the HERA experiments ZEUS and H1 on structure functions are summarized in section 10, and section 11 contains the conclusions.

2 Deep Inelastic Scattering – Basic Notations

The deep inelastic scattering cross sections for charged lepton– $l^{\pm}p(n) \to l'X$, ($l^{\pm} = e^{\pm}, \mu^{\pm}$) and neutrino–nucleon scattering $\nu(\overline{\nu})p(n) \to l'X$ are described by three basic variables:

$$Q^2 = -(l-l')^2 = -(p_{q_i} - p_{q_f})^2, \quad x_B \equiv x = \frac{Q^2}{2P.q}, \quad y_B \equiv y = \frac{q.P}{l.P} = \frac{\nu M}{l.P} \tag{1}$$

in the Born–approximation. Here, l and l' denote the incoming and outgoing lepton momenta, p_{q_i} and p_{q_f} are the momenta of the incoming and outgoing struck quark, q is the four momentum transfer from the lepton to the quark side, P is the nucleon momentum, and M the nucleon mass. In the nucleon rest frame one obtains $\nu = E_l y$.

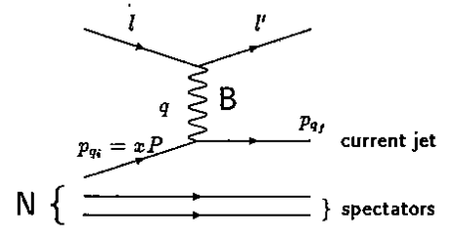

Figure 1: Diagram describing deep inelastic $lN \to l'X$ scattering for neutral and charged current processes. The exchanged boson B may be a photon, $Z-$ or $W^{\pm}$ boson, and $N = p, n$, $l = e^{\pm}, \mu^{\pm}, \nu_{e,\mu}$ and $\overline{\nu}_{\mu,e}$.

The diagram describing the process is shown in Figure 1. Here, $Q^2 = -q^2$ is the virtuality of the exchanged boson: γ or Z for neutral current and $W^{\pm}$ for charged current reactions. The Bjorken variables x and y are related to Q^2 by $Q^2 = xys$, with $s = (P+l)^2$ the cms energy. y denotes the energy transfer of the initial state lepton to the hadronic system in the rest frame of the target. x has a physical interpretation in the parton model [3]. It denotes the 4–momentum fraction of the struck–parton (quark) in the infinite momentum frame.

Basically there are eight types of deep inelastic reactions:

$$\begin{array}{lcl} l^{\pm}N & \to & l^{\pm}X \\ l^{\pm}N & \to & \overline{\nu}(\nu)X \\ \nu(\overline{\nu})N & \to & \nu(\overline{\nu})X \\ \nu(\overline{\nu})N & \to & l^{-}(l^{+})X \end{array} \tag{2}$$

with $N = p$ or n. The differential cross sections for these processes are given by

$$\frac{d^2\sigma_{nc}^{l^{\pm}N}}{dxdQ^2} = \frac{2\pi\alpha^2}{Q^4}\frac{Msy}{x\left(s-M^2\right)^2}\left\{L_{\gamma\gamma}^{\mu\nu}W_{\mu\nu}^{\gamma\gamma} + \kappa_Z(Q^2)\left[L_{\gamma Z}^{\mu\nu}W_{\mu\nu}^{\gamma Z} + L_{Z\gamma}^{\mu\nu}W_{\mu\nu}^{Z\gamma}\right] + \kappa_Z^2(Q^2)L_{ZZ}^{\mu\nu}W_{\mu\nu}^{ZZ}\right\}$$

$$
\begin{aligned}
\frac{d^2\sigma_{cc}^{l^\pm N}}{dxdQ^2} &= 2\pi\alpha^2 \frac{Msy}{x\,(s-M^2)^2}\frac{1}{(Q^2+M_W^2)^2} L^{\mu\nu}_{W^\pm W^\mp} W_{\mu\nu}^{W^\pm W^\mp} \\
\frac{d^2\sigma_{nc}^{\nu(\overline{\nu})N}}{dxdQ^2} &= \frac{G_F^2 M_W^4}{4\pi}\frac{Msy}{x\,(s-M^2)^2}\frac{1}{(Q^2+M_Z^2)^2} L^{\mu\nu}_{ZZ} W_{\mu\nu}^{ZZ} \\
\frac{d^2\sigma_{cc}^{\nu(\overline{\nu})N}}{dxdQ^2} &= \frac{G_F^2 M_W^4}{4\pi}\frac{Msy}{x\,(s-M^2)^2}\frac{1}{(Q^2+M_W^2)^2} L^{\mu\nu}_{W^\pm W^\mp} W_{\mu\nu}^{W^\pm W^\mp}
\end{aligned} \tag{3}
$$

with

$$
\kappa_Z(Q^2) = \frac{1}{4\sin^2\theta_w\cos^2\theta_w}\frac{Q^2}{Q^2+M_Z^2} \quad \text{and} \quad \frac{G_F^2 M_W^4}{4\pi} = \frac{2\pi\alpha^2}{16\sin^4\theta_w}. \tag{4}
$$

The last relation can be used to rewrite the last two equations in (3). Here, α denotes the electromagnetic fine structure constant, $M_{Z,W}$ are the masses of the weak gauge bosons, G_F is the Fermi constant, and θ_w denotes the electroweak mixing angle. The leptonic[1] $L_{\mu\nu}^{\alpha\beta}$ and hadronic tensors $W_{\mu\nu}^{\alpha\beta}$ are:

$$
\begin{aligned}
L_{\mu\nu}^{\gamma\gamma} &= 2\left[l_\mu l'_\nu + l'_\mu l_\nu - g_{\mu\nu} l.l'\right] \\
L_{\mu\nu}^{\gamma Z} &= 2v\left[l_\mu l'_\nu + l'_\mu l_\nu - g_{\mu\nu} l.l'\right] + 2ia\varepsilon_{\mu\nu\alpha\beta} l^\alpha l'^\beta \\
L_{\mu\nu}^{Z\gamma} &= 2v\left[l_\mu l'_\nu + l'_\mu l_\nu - g_{\mu\nu} l.l'\right] - 2ia\varepsilon_{\mu\nu\alpha\beta} l^\alpha l'^\beta \\
L_{\mu\nu}^{ZZ} &= 2(\hat{v}^2+\hat{a}^2)\left[l_\mu l'_\nu + l'_\mu l_\nu - g_{\mu\nu} l.l'\right] \mp 4i\hat{v}\hat{a}\varepsilon_{\mu\nu\alpha\beta} l^\alpha l'^\beta \\
L_{\mu\nu}^{W^\pm W^\mp} &= 2\left[l_\mu l'_\nu + l'_\mu l_\nu - g_{\mu\nu} l.l' \mp i\varepsilon_{\mu\nu\alpha\beta} l^\alpha l'^\beta\right]
\end{aligned} \tag{5}
$$

where $\hat{v}$ and $\hat{a}$ are the axial and vector couplings of the electron and neutrino, respectively.

$$
\hat{v} \equiv v = -\frac{1}{2} + 2\sin^2\theta_w \quad \hat{a} \equiv a = -\frac{1}{2} \quad \text{or} \quad \hat{v} \equiv v_\nu = \frac{1}{2} \quad \hat{a} \equiv a_\nu = \frac{1}{2} \tag{6}
$$

and

$$
\begin{aligned}
W_{\mu\nu}^{\gamma\gamma} &= \frac{1}{4\pi}\sum_n \langle P|J_\mu^{\gamma\dagger}(0)|n\rangle\langle n|J_\nu^{\gamma}(0)|P\rangle (2\pi)^4\delta^{(4)}(P+q-p_n) \\
W_{\mu\nu}^{\gamma Z} &= \frac{1}{4\pi}\sum_n \langle P|J_\mu^{\gamma\dagger}(0)|n\rangle\langle n|J_\nu^{Z}(0)|P\rangle (2\pi)^4\delta^{(4)}(P+q-p_n) \\
W_{\mu\nu}^{Z\gamma} &= \frac{1}{4\pi}\sum_n \langle P|J_\mu^{Z\dagger}(0)|n\rangle\langle n|J_\nu^{\gamma}(0)|P\rangle (2\pi)^4\delta^{(4)}(P+q-p_n) \\
W_{\mu\nu}^{ZZ} &= \frac{1}{4\pi}\sum_n \langle P|J_\mu^{Z\dagger}(0)|n\rangle\langle n|J_\nu^{Z}(0)|P\rangle (2\pi)^4\delta^{(4)}(P+q-p_n) \\
W_{\mu\nu}^{W^\pm W^\mp} &= \frac{1}{4\pi}\sum_n \langle P|J_\mu^{W^\pm\dagger}(0)|n\rangle\langle n|J_\nu^{W^\mp}(0)|P\rangle (2\pi)^4\delta^{(4)}(P+q-p_n)
\end{aligned} \tag{7}
$$

Assuming Lorentz invariance the hadronic tensors may be expressed in terms of six independent structure functions[2] $W_i(x,Q^2)$ [4], which differ in general for the processes considered.

[1] Here, the lepton masses have been neglected. The upper (lower) sign in (5d) refers to $e^-(e^+)$ and $\nu(\overline{\nu})$ coupling.

[2] They correspond to the six tensorial (or pseudotensorial) quantities: $P_\mu P_\nu$, $P_\mu q_\nu$, $q_\mu P_\nu$, $q_\mu q_\nu$, $g_{\mu\nu}$, and $\varepsilon_{\mu\nu\alpha\beta}P^\alpha q^\beta$ which may be formed from the 4-vectors determining $W_{\mu\nu}$.

$$
\begin{aligned}
W_{\mu\nu} &= \left(-g_{\mu\nu} + \frac{q_\mu q_\nu}{q^2}\right) W_1(x,Q^2,\nu) + \frac{1}{M^2}\left[\left(P_\mu - \frac{P.q}{q^2}q_\mu\right)\left(P_\nu - \frac{P.q}{q^2}q_\nu\right)\right] W_2(x,Q^2,\nu) \\
&- \frac{i}{2M^2}\varepsilon_{\mu\nu\alpha\beta}P^\alpha q^\beta W_3(x,Q^2,\nu) + \frac{1}{M^2} q_\mu q_\nu W_4(x,Q^2) \\
&+ \frac{1}{M^2}\left[P_\mu q_\nu + q_\mu P_\nu\right] W_5(x,Q^2,\nu) + \frac{i}{M^2}\left[P_\mu q_\nu - q_\mu P_\nu\right] W_6(x,Q^2,\nu)
\end{aligned} \tag{8}
$$

The last term in (8) does not contribute to the Born cross section, because the contraction with all lepton tensors listed in (5) vanishes[3]. Similarly, one finds that the terms $\propto W_{4,5}(x,Q^2)$ are proportional to m_l^2 because of $L_{\mu\nu}q^{\nu(\mu)} = m_l^2 l_{\mu(\nu)}$. Thus, the cross sections may be described by effectively three structure functions [4]. From (8) the structure functions can be derived by the following projections

$$
\begin{aligned}
W_2(x,Q^2,\nu) &= x\left(-g_{\mu\nu} + \frac{12x^2}{Q^2}P_\mu P_\nu\right) W^{\mu\nu} \\
W_L(x,Q^2,\nu) &= W_2(x,Q^2,\nu) - 2xW_1(x,Q^2,\nu) = \frac{8x^3}{Q^2}P_\mu P_\nu W^{\mu\nu} \\
xW_3(x,Q^2,\nu) &= \frac{ixP^\rho q^\sigma \varepsilon_{\mu\nu\rho\sigma}}{[Q^2+(P.q)^2/M^2]} W^{\mu\nu}
\end{aligned} \tag{9}
$$

In the Bjorken limit [5]:

$$
x = \text{const.} \qquad Q^2, \nu \to \infty \tag{10}
$$

the structure functions $W_{1,2,3}$ depend only on two variables:

$$
\begin{aligned}
\lim_{Bj} MW_1(x,Q^2,\nu) &= F_1(x,Q^2) \\
\lim_{Bj} \nu W_2(x,Q^2,\nu) &= F_2(x,Q^2) \\
\lim_{Bj} \nu W_3(x,Q^2,\nu) &= F_3(x,Q^2)
\end{aligned} \tag{11}
$$

The cross sections (3) may hence be rewritten correspondingly. In the case of pure photon exchange $Q^2 \ll M_Z^2$ the cross section $d^2\sigma_{nc}^{l^\pm N}/dxdQ^2$ reads [5]

$$
\frac{d^2\sigma}{dxdQ^2} = \frac{2\pi\alpha^2}{xQ^4}\left[y^2 2xF_1(x,Q^2) + 2(1-y)F_2(x,Q^2)\right] \tag{12}
$$

$$
\simeq \frac{2\pi\alpha^2}{xQ^4} Y_+ F_2(x,Q^2) \quad \text{for} \quad F_L = F_2 - 2xF_1 \simeq 0 \tag{13}
$$

with $Y_\pm = 1 \pm (1-y)^2$. Neglecting the longitudinal structure functions[6] the differential cross sections for neutral and charged current $l^\pm N$ deep inelastic scattering are given by

$$
\frac{d^2\sigma_{nc}^{\pm}}{dxdQ^2} = \frac{2\pi\alpha^2}{xQ^4}\left\{Y_+ \mathcal{F}_2^\pm(x,Q^2) + Y_- \mathcal{F}_3^\pm(x,Q^2)\right\} \tag{14}
$$

[3] This contribution to $W_{\mu\nu}$ is antisymmetric. Since $q = l - l'$ one obtains $\varepsilon_{\mu\nu\alpha\beta}l^\alpha l'^\beta(P_\mu q_\nu - q_\mu P_\nu) = 0$.

[4] This conclusion is a consequence of vector-boson exchange. If in the range of high Q^2 new bosons coupling to leptons and hadrons are found, the hadronic tensor may have a different representation.

[5] Because of the parity conservation of the electromagnetic current the decomposition of $W_{\mu\nu}^{\gamma\gamma}$ does not contain a W_3 term.

[6] These functions will be considered in section 7.1 in detail. They contribute with $\mathcal{O}(\alpha_s)$ only [6].

$$\mathcal{F}_2^{\pm}(x,Q^2) = F_2(x,Q^2) + \kappa_Z(Q^2)(-v \mp \lambda a)G_2(x,Q^2) + \kappa_Z^2(Q^2)(v^2+a^2 \pm 2\lambda va)H_2(x,Q^2) \quad (15)$$

$$\mathcal{F}_3^{\pm}(x,Q^2) = \kappa_Z(Q^2)(\pm a + \lambda v)xG_3(x,Q^2) + \kappa_Z(Q^2)^2[\mp 2va - \lambda(v^2+a^2)]xH_3(x,Q^2) \quad (16)$$

with and λ denotes the polarization of the positron and electron beams, respectively. The representations of the different structure functions within the parton model will be given in section 6. The charged current differential cross sections are

$$\frac{d^2\sigma_{cc}^{\pm}}{dxdQ^2} = \frac{2\pi\alpha^2}{xQ^4}\kappa_W^2(Q^2)\left(\frac{1\pm\lambda}{2}\right)\left\{Y_+W_2^{\pm}(x,Q^2) \mp Y_-xW_3^{\pm}(x,Q^2)\right\} \quad (17)$$

where

$$\kappa_W(Q^2) = \frac{1}{4\sin^2\theta_w}\,\frac{Q^2}{Q^2+M_W^2} \quad (18)$$

Finally, the cross sections for the corresponding neutrino reactions read:

$$\frac{d^2\sigma_{nc}^{\nu,\bar{\nu}}}{dxdQ^2} = \frac{G_F^2M_W^4}{4\pi xQ^4}\,\frac{Q^4}{(Q^2+M_Z^2)^2}\left\{Y_+\widehat{F}_2^{\nu,\bar{\nu}}(x,Q^2) \pm Y_-x\widehat{F}_3^{\nu,\bar{\nu}}(x,Q^2)\right\} \quad (19)$$

$$\frac{d^2\sigma_{cc}^{\nu,\bar{\nu}}}{dxdQ^2} = \frac{G_F^2M_W^4}{4\pi xQ^4}\,\frac{Q^4}{(Q^2+M_W^2)^2}\left\{Y_+\widehat{W}_2^{\nu,\bar{\nu}}(x,Q^2) \pm Y_-x\widehat{W}_3^{\nu,\bar{\nu}}(x,Q^2)\right\} \quad (20)$$

3 Kinematics and Eventrates

To compare the potential of different present and future high energy lepton–hadron scattering experiments to measure the nucleon structure functions, we will first summarize typical characteristics as the kinematical ranges to be probed, available integrated luminosities, and corresponding charged and neutral current event rates. For definiteness we will compare the possibilities at HERA, at LEP $\otimes$ LHC, and of a high energy νN fixed target experiment [7].

The design parameters for the electron and proton beams at HERA are $E_p = 820\,\mathrm{GeV}$ and $E_e = 30\,\mathrm{GeV}$. The physics program definitely requires runs at lower cms energies also, e.g. to unfold both the structure functions $F_2(x,Q^2)$ and $F_L(x,Q^2)$ from the measured differential neutral current cross section and to fill the range of higher x values at a given Q^2 appropriately. Therefore, we will consider also a low energy option $E_p = 300\,\mathrm{GeV}$ and $E_e = 10\,\mathrm{GeV}$ in accord with the parameters of HERA. Currently only e^-p collisions are investigated. However, with similar luminosities also e^+p runs are possible. Furthermore, scattering off deuteron targets may be studied in future. When the design luminosity is reached the integrated luminosity per year amounts to about $\mathcal{L} = 100\ pb^{-1}$.

At a possible future eN facility at LEP $\otimes$ LHC similar investigations can be performed. A high energy option of $s = 4E_pE_e \simeq 4\cdot 8000\cdot 100\,\mathrm{GeV}^2$ at $\mathcal{L} = 100\ pb^{-1}/\mathrm{yr}$ and a low energy option with $s = 4\cdot 2000\cdot 50\,\mathrm{GeV}^2$ at $\mathcal{L} = 1\ fb^{-1}/\mathrm{yr}$ have been discussed in [8]. Both electron and positron beams, and aside proton beams also deuteron beams, may be used similarly to the case of HERA.

At a fixed target neutrino facility the neutrino and antineutrino beams are derived from a high energy proton beam, which is dumped on a target. For the example of a 3 TeV initial proton beam energy spectra for neutrino and antineutrino beams with $\langle E_{\nu,\bar{\nu}}\rangle = 400...700\,\mathrm{GeV}$ may be reached depending on the magnetic system applied [7]. To compare deep inelastic scattering under similar conditions as in the case of $e^{\pm}p(d)$ at HERA and LEP $\otimes$ LHC, ν–scattering off H_2 and D_2 tank targets is considered allowing a simultaneous measurement of νp and νd interactions. A periodic interchange of the positions of the H_2 and D_2 tanks minimizes systematic influences due to the target position. The lay–out of a corresponding experimental set–up is depicted in figure 2.

The neutrino and antineutrino fluxes are estimated to be $\Phi_\nu = 2.4\cdot 10^{-3}\ ...\ 10^{-4} m^{-2}\mathrm{proton}^{-1}$ at a bunch intensity of 10^{14} protons per cycle and a cycle period of $\tau \approx 120\,\mathrm{sec}$. The (anti)neutrino energy spectra are shown in figure 3.

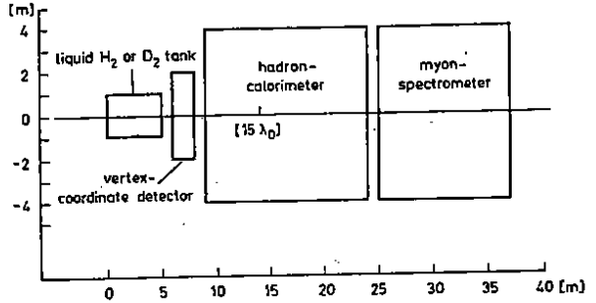

Figure 2: Schematic lay–out of a neutrino experiment using H_2 and D_2 tank targets [7].

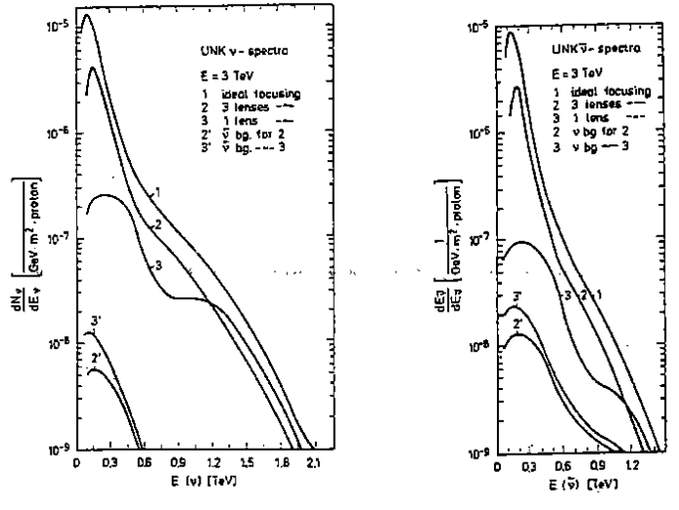

Figure 3: Energy spectra for neutrino and antineutrino wide band beams [7].

The accessible kinematical ranges for the design parameters, a low, and a high energy option at HERA are depicted in Figure 4. For $Q^2 \gtrsim 10\,\mathrm{GeV}^2$ x values $x \sim 10^{-4}$ may be reached. It is seen in figure 4 that the low energy option allows to fill a gap left in the case of the design option,

[7] Estimates for such an experiment have been derived some time ago in [7] for a neutrino experiment at the planned UNK neutrino facility. The neutrino and antineutrino beams were assumed to be derived from a 3 TeV proton beam. The basic conclusions from this study apply also to possible future fixed target neutrino facilities at other proton colliders in a similar energy range.

and, furthermore, the kinematical range is extended towards larger x which will turn out to be very important for the QCD analysis (see section 8).

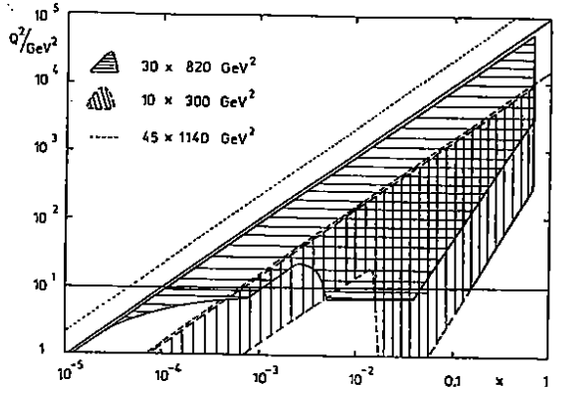

Figure 4: Accessible kinematic (x, Q^2) ranges at HERA for minimum and design energies E_p and E_e. Note that for $Q^2 \geq 10\,\mathrm{GeV}^2$ the extension towards the fixed target region at large x is achieved by lowering the proton beam energy only, [9].

The kinematical ranges, which may be probed at LEP $\otimes$ LHC are shown in figure 5. At $Q^2 \geq 10\,\mathrm{GeV}^2$ one may reach even values of $x \sim 10^{-5}$ using the electron measurement. In this way the range accessible at HERA may be extended by one order of magnitude. Note, that also the range towards high values of Q^2 will be extended considerably.

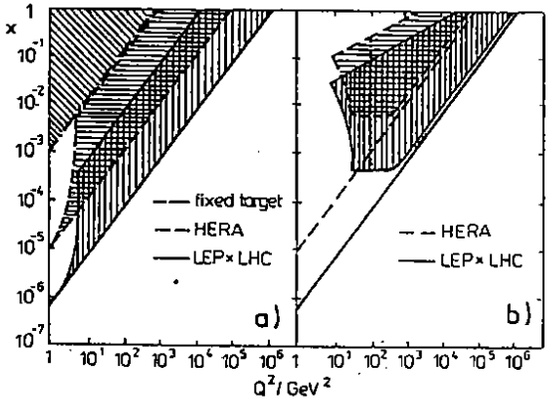

Figure 5: Kinematical ranges at LEP $\otimes$ LHC. range obtained via a) $e^{\pm}$ measurement; b) jet measurement, [8].

Contrary to this, the accessible domain in x and Q^2 which may be obtained by the neutrino experiment described above will range only to $x \sim 4 \cdot 10^{-3}$ at $Q^2 = 10\,\mathrm{GeV}^2$ and to a few 10^3 GeV^2 in Q^2 at a sufficient statistics (see figure 6). However, these data may allow to derive quark distribution function of different flavours in a range not covered sufficiently neither by HERA nor LEP $\otimes$ LHC.

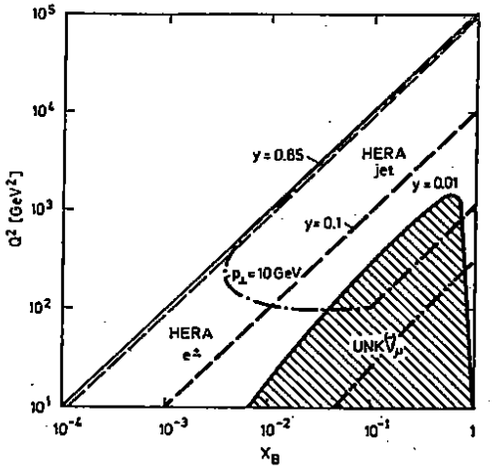

Figure 6: Comparison of the $x - Q^2$ range at SPS, UNK and HERA. Below the lower dash–dotted line: SPS range; shaded area: νN range (3 TeV p–beam). The dashed line indicates the range accessible via the electron measurement, the dash–dotted line the range of the jet measurement at HERA for $s = 10^5\,\mathrm{GeV}^2$, [7].

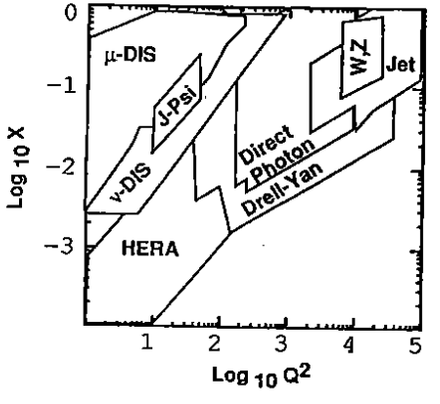

Figure 7: Kinematical range in x and Q^2 accessible in present hard scattering experiments, [10].

It may be instructive to ask to which extent also the measurement of other hard processes in past and present experiments contains information on parton distributions, which could be derived

by global analyses. A compilation of those processes has been performed some time ago [10]. Aside of deep inelastic $\mu^{\pm}N, e^{\pm}N$ and νN interactions, Drell–Yan data, direct photon data, W and Z production, J/ψ production and hard jet production cross sections may be used to extract parton distributions.

The about ranges for the different processes are depicted in figure 7. The measurement of structure functions at HERA thus yields access to the smallest x values currently, while the highest p_T values are reached studying jet and W, Z production at hadron colliders.

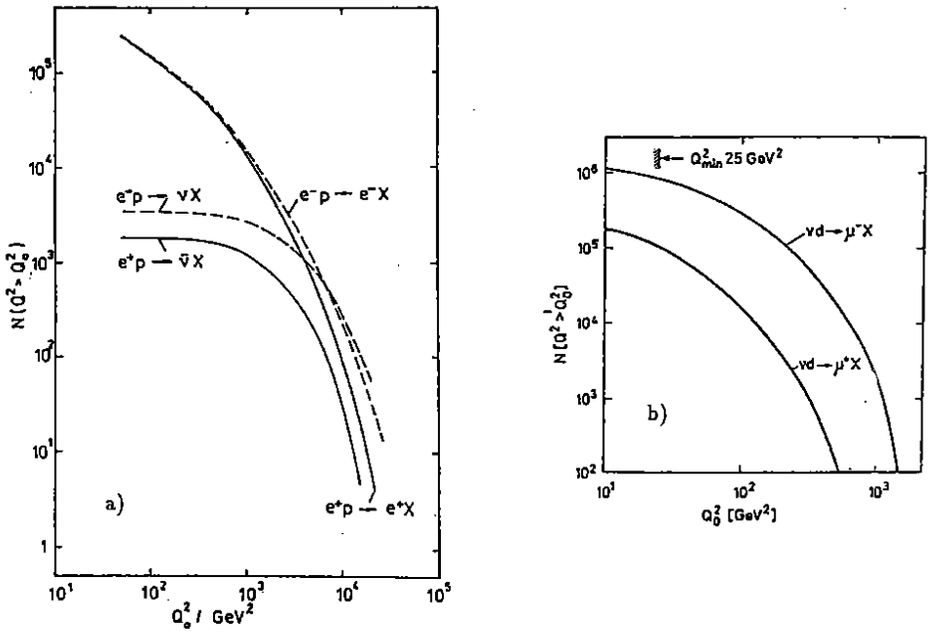

Figure 8: a) Neutral and charged current event rates for $Q^2 \geq Q_0^2$, $x \geq 0.01$, $y \geq 0.03$, $\mathcal{L} = 100 pb^{-1}$, and $\sqrt{s} = 314\,\mathrm{GeV}$ at HERA, [11]; b) integrated charged current event rates for the p/d neutrino facility (see text) for neutrino and antineutrino–deuterium interactions, [7].

The event rates which may be collected under the above assumptions are compared in figures 8 and 9 for HERA, the neutrino experiment, and LEP $\otimes$ LHC. For $Q^2 \geq 20\,\mathrm{GeV}^2$ and $x \geq 10^{-2}$ a typical amount of neutral current deep inelastic data of a few 10^5 events is reached in the experiments at HERA. However, in the range below $x = 10^{-2}$ several millions of events are obtained at the same time. Contrary to this the charged current statistics ranges to a few 10^3 events only which are situated at $Q^2 \gtrsim 500\,\mathrm{GeV}^2$. Only in the range $Q^2 \gtrsim 1000\,\mathrm{GeV}^2$ both samples become of comparable order, however, not at high statistics. This limits the investigation of the range of high Q^2 to values of $Q^2 \lesssim 20.000\,\mathrm{GeV}^2$ practically.

The p/d neutrino facility, on the other hand, may take between 10^5 and 10^6 events for

$Q^2 \geq 10\,\mathrm{GeV}^2$. These data range, however, at a rate of 100 events only to about $Q^2 \sim 1000\,\mathrm{GeV}^2$.

The neutral and charged current event rates for deep inelastic scattering at LEP $\otimes$ LHC are illustrated in figure 9 as a function of minimal x and Q^2 values. At an integrated luminosity of $\mathcal{L} = 1\ fb^{-1}$ the statistics of charged and neutral current events becomes of similar size for Q^2 of $\mathcal{O}(10^4\ \mathrm{GeV}^2)$ amounting to $\sim 10^5$ events.

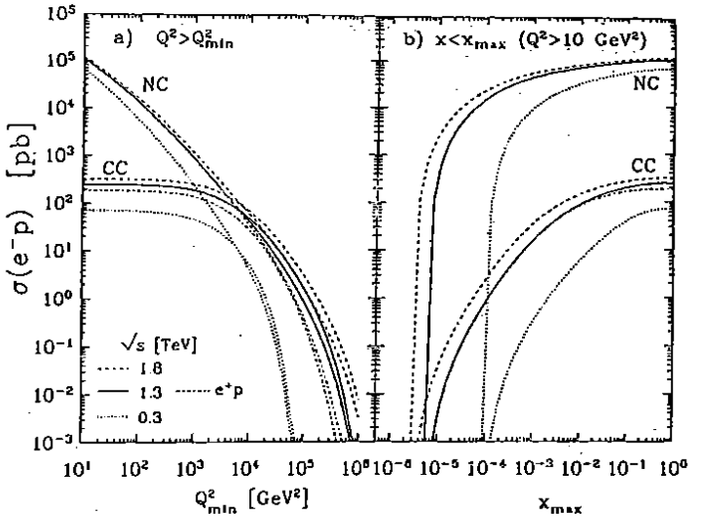

Figure 9: Integrated DIS e^-p cross sections versus (a) a lower cut–off in Q^2 and (b) an upper cut–off in x. Charged and neutral current interactions are compared for different e^-p cms energies corresponding to LEP $\otimes$ LHC and HERA; only one e^+p energy for clarity, [12].

4 QED Radiative Corrections

The QED radiative corrections yield potentially large contributions to the measured deep inelastic scattering cross sections in lepton–nucleon reactions. The measurement of the structure functions, unfolding of parton distributions, and QCD tests require to correct for these contributions. During the last years the $\mathcal{O}(\alpha)$ radiative corrections were calculated by different groups and agreement of the different approaches at the per cent level or better has been obtained [13]. The QED corrections were derived in semi–analytical calculations [14, 15] , Monte Carlo approaches [16], and using the leading log approximation [17]–[23].

As shown by different comparisons (see e.g. [13]) the QED radiative corrections are to a wide extent described by the contributions obtained in the leading log approximation, which is basically due to the fact that terms of $\mathcal{O}(1)$ may be neglected in comparison with the 'large' logs $\sim \ln(Q^2/m_f^2)$, with m_f being the mass of the radiating fermion. Here, we will consider the leading log approximation as a pedagogical view of the problem also, which allows to find the relevant contributions in a very transparent way.

In the leading log approach only terms are considered which are associated with mass singularities. These terms arise from collinear emissions of photons off (massless) charged fermions. For the process of deep inelastic scattering there are (up to) four contributions due to bremsstrahlung in $\mathcal{O}(\alpha)$: initial state bremsstrahlung (isr) off electrons (muons) or (massless) quarks and final state bremsstrahlung (fsr) off charged leptons or quarks. The contributing diagrams are depicted generically in figure 10. Furthermore, the corresponding virtual and soft terms have to be added. In logarithmic order the contributions can be associated with the single bremsstrahlung diagrams individually. These terms are described by the non–singlet splitting function for a fermion–fermion transition:

$$P_{ff}(x) = \delta(1-x) + \frac{\alpha e_f^2}{2\pi} \log\left(\frac{Q^2}{m_f^2}\right) \left\{ \frac{1+x^2}{1-x} + \frac{3}{2}\delta(1-x) \right\} + \mathcal{O}(\alpha^2) \tag{21}$$

Due to the Weierstrass' polynomial theorem and the conservation of probability one has

$$\int_0^1 dx P_{ff}^{(0)}(x) = 1 \quad \text{and} \quad \int_0^1 dx P_{ff}^{(1)}(x) = 0 \tag{22}$$

where (n) denotes the order in α.

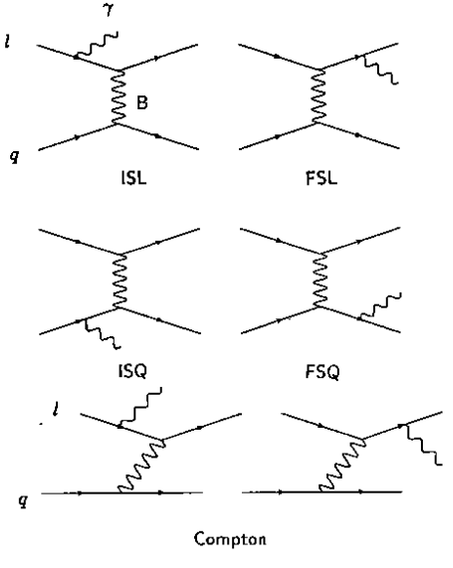

Figure 10: Diagrams describing collinear bremsstrahlung of photons off (massless) fermions for $l^{\pm}N$ scattering.

The contributions due to isr and fsr from light leptons ($l = e^{\pm}, \mu^{\pm}$) are thus given by

$$\frac{d\sigma_l^{(1)}}{dxdy} = \frac{\alpha}{2\pi} \ln\left(\frac{Q^2}{m_l^2}\right) \int_0^1 dz \frac{1+z^2}{1-z} \left\{ \theta(z-z_0) \frac{d^2\sigma^{(0)}}{dxdy}\bigg|_{x=\hat{x},y=\hat{y},s=\hat{s}} |\mathcal{J}(x,y,s)| - \frac{d^2\sigma^{(0)}}{dxdy} \right\} \tag{23}$$

where the Jacobian $\mathcal{J}$ reads

$$\mathcal{J}(x,y,s) = \begin{vmatrix} \partial\hat{x}/\partial x & \partial\hat{x}/\partial y \\ \partial\hat{y}/\partial x & \partial\hat{y}/\partial y \end{vmatrix} \tag{24}$$

Eq. (23) describes the contributions to the deep inelastic Born cross sections treating the irradiated photon inclusively, i.e. unobserved. Correspondingly, the outer kinematical variables x, y, and Q^2 depend on the way in which they have been measured, since they refer to a $2 \to 2$ process. In the past three situations were considered[8]:

i) lepton measurement: Q^2 and y defined at the leptonic vertex
ii) jet measurement: Q^2 and y defined at the hadronic vertex
iii) mixed variables: Q^2 measured at the leptonic and y measured at the hadronic vertex.

In the case of jet measurement the kinematical variables are defined using the Jaquet–Blondel method.

The so–called 'shifted' variables occuring in eq. (23) $\hat{x}$, $\hat{y}$ and $\hat{s}$ are given by

$$\begin{array}{lllll} \text{initial state radiation} & \hat{y} = (z+y-1)/z & \hat{Q}^2 = Q^2 z & \hat{s} = sz \\ \text{final state radiation} & \hat{y} = (z+y-1)/z & \hat{Q}^2 = Q^2/z & \hat{s} = s/z \end{array} \tag{25}$$

in the case of lepton measurement, with $\hat{x} = \hat{Q}^2/\hat{s}\hat{y}$, and $\hat{x}(z_0) = 1$.

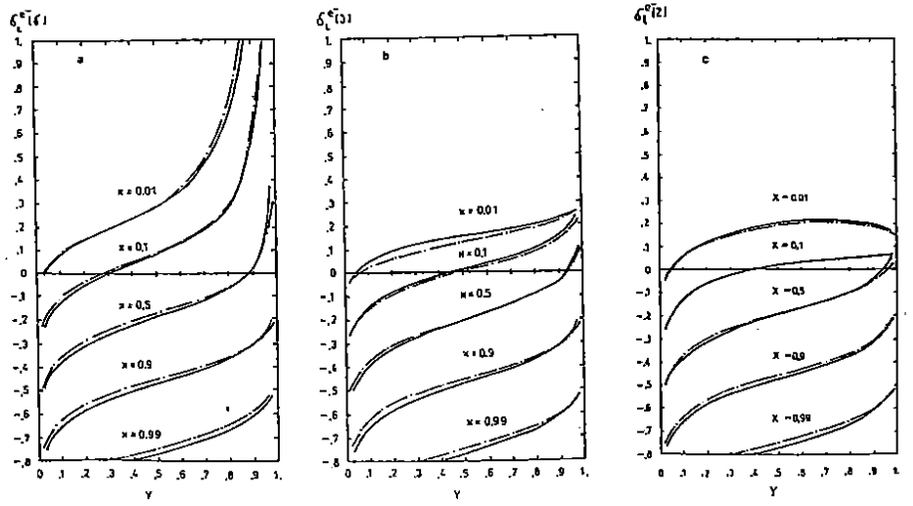

Figure 11: Relative LLA QED corrections in $\mathcal{O}(\alpha)$ for the photon exchange term (a), $\gamma - Z$ interference term (b), and the Z exchange term for neutral current deep inelastic scattering at $\sqrt{s} = 314$ GeV (full lines) (c). For comparison the result of a full calculation [15] is shown (dash–dotted lines); from [17].

[8]The ZEUS collaboration uses two other methods currently: the double–angle method and the reconstruction of the kinematic variables from the measurement of the electron scattering angle and y_B measured at the hadronic vertex. The leading log radiative corrections for these variables (up to $\mathcal{O}(\alpha^2)$) have been calculated in [21]. In the small–x range $x \leq 10^{-2}$ the correction turns out to be smaller than 3 % in the case of the double–angle method.

Due to the finite resolution of the electromagnetic calorimeter measuring the electromagnetic (e',γ) final state it may be difficult to resolve the final state photon from the electron in practice. According to the Kinoshita–Lee–Nauenberg (KLN) theorem [24] the fsr term vanishes in this case.

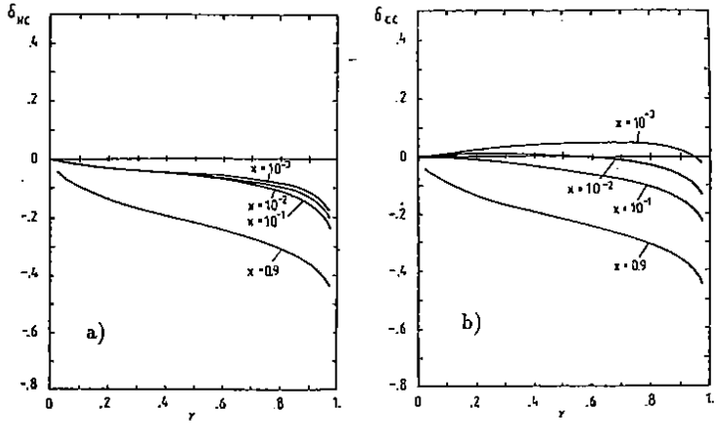

Figure 12: $\mathcal{O}(\alpha)$ leading log QED corrections to deep inelastic scattering using jet measurement at $\sqrt{s}$ = 314 GeV in dependence of x and y. a) neutral current scattering; b) charged current scattering, [20].

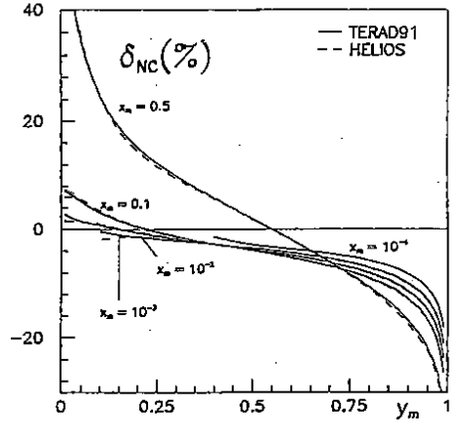

Figure 13: QED leptonic corrections to $d\sigma/dxdy$ for mixed variables in per cent. Full lines are complete $\mathcal{O}(\alpha)$ results from TERAD91 [25], the dashed lines represent results from the leading logarithmic approximation (see [20]) obtained from HELIOS [23]; from [13].

For the case of jet measurement and mixed variables the shifted variables are:

jet measurement	$\hat{y} = y/z$	$\hat{Q}^2 = Q^2(1-y)/(1-y/z)$	$\hat{s} = sz$	$\hat{x}(z_0) = 1$
mixed variables (isr)	$\hat{y} = y/z$	$\hat{Q}^2 = Q^2 z$	$\hat{s} = sz$	$z_0 = y$
mixed variables (fsr)	$\hat{y} = y$	$\hat{Q}^2 = Q^2/z$	$\hat{s} = s$	$z_0 = x$

(26)

Note, that in the case of jet measurement a fsr term does not contribute due to the KLN–theorem.

A comparison of figures 11–13 shows, that the leptonic QED corrections are widely different depending on the type of outer variables used. For lepton measurement they are particularly huge at small x and high y, while for jet measurement and the case of mixed variables and small x they behave flat in y and are much smaller. Note also the good agreement of the results of the full and LLA calculation which is illustrated in figure 11 and 13 and holds also for the case of jet measurement [26].

The contribution due to isr from a quark line may be considered together with gluon bremsstrahlung. The latter contributes to the scaling violations of the quark distributions. Similarly, the photon emission may be considered as a corresponding QED contribution which modifies the fermion–fermion splitting function of the evolution equation (see sect. 8) [27] by

$$P_{ff}(z,Q^2) \Longrightarrow \left(1 + \frac{\alpha}{C_F \alpha_s(Q^2)}\right) \frac{1+z^2}{1-z} \tag{27}$$

with $\delta_{ik} C_F = \sum_{a,j} t^a_{ij} t^a_{jk} = \delta_{ik}(4/3)$. This effect is of the order of a few per cent only [28].

In the case of lepton measurement a large contribution to the radiative corrections is caused by the Compton–term [17, 18, 29, 30] (see figure 10). The nearly collinear emission of the virtual photon off a quark line accompanied by wide angle photon emission of the leptons yields

$$\frac{d^2\sigma_{Compton}}{dxdy} = \frac{\alpha^3}{sx} \sum_f \log\left(\frac{Q^2}{\Lambda^2}\right) \int_x^1 \frac{dz}{z^3} z \left[q_f(z,Q^2) + \bar{q}_f(z,Q^2)\right] \frac{z^2 + (x-z)^2}{x(1-y)} Y_+ \tag{28}$$

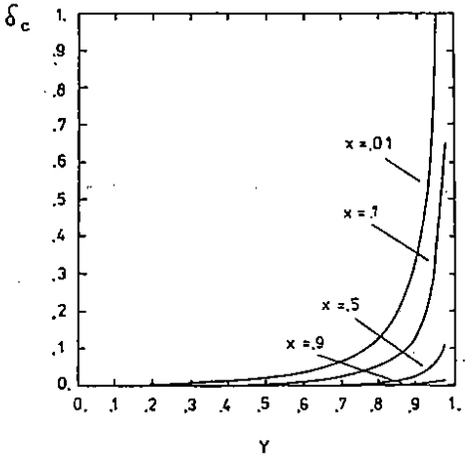

Figure 14: $(d^2\sigma_{Compton}/dxdy/d^2)(\sigma_0/dxdy)$ due to $\gamma^* e \to \gamma e$ scattering as a function of x and y (28) with Λ = 200 MeV, [17].

The signature of these events is characterized by an electron–photon pair being nearly balanced in p_T and a rather low hadronic activity. As shown in [30] one can widely isolate this event sample and one may use these events to measure the nucleon structure functions at small x and small Q^2, i.e. in an entirely nonperturbative region.

QED radiative corrections for $\nu(\bar{\nu})N$ deep inelastic scattering have been calculated in [31, 27]. The leptonic final state corrections are in general smaller than in the case of $e^{\pm}N$ scattering because the exchanged boson ($W^{\pm}$) is massive. Furthermore, for $\nu_\mu N$ scattering the correction is suppressed also due to the larger mass of the final state fermion.

For the leptonic corrections the leading log calculation has been also performed up to $\mathcal{O}(\alpha^2)$ for the case of lepton measurement [22] and other kinematical variables [21].

5 Ways to extract Structure Functions

5.1 $l^{\pm}N$

Structure functions can be measured forming suitable linear combinations of the deep inelastic scattering cross sections:

$$\hat{\sigma}^{\pm}_{nc,cc} := \frac{d\sigma^{\pm}_{nc,cc}}{dxdQ^2} \tag{29}$$

Because the number of structure functions is larger than the number of measurable differential cross sections not all structure functions can be determined.

For neutral current $l^{\pm}N$ scattering one may form the combination

$$\begin{aligned} B_+(\lambda) &= \frac{1}{2}\left[\hat{\sigma}^+_{nc}(-\lambda) + \hat{\sigma}^-_{nc}(+\lambda)\right]\frac{1}{Y_+}\frac{xQ^4}{2\pi\alpha^2} \\ &= F_2 + (-v+\lambda a)\kappa_Z G_2 + (v^2+a^2-2va\lambda)\kappa_Z^2 H_2 \end{aligned} \tag{30}$$

Here, λ denotes the longitudinal lepton beam polarization. The term $-v+\lambda a$ can be choosen to vanish tuning the beam polarization[9].

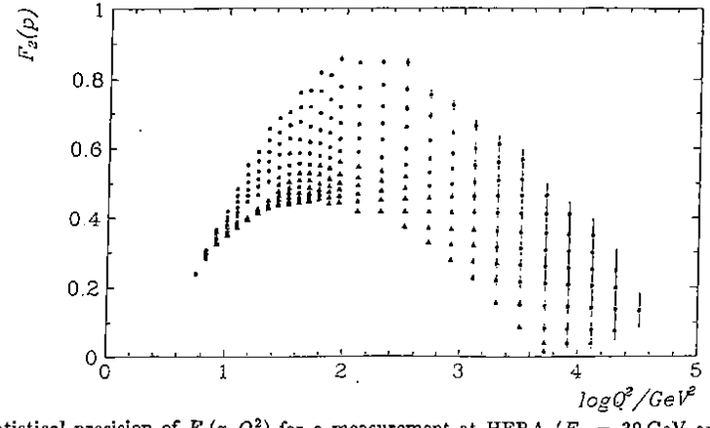

Figure 15: Statistical precision of $F_2(x,Q^2)$ for a measurement at HERA (E_e = 30 GeV and E_p = 820 GeV), $\mathcal{L} = 100pb^{-1}$, assuming the KMRS B^0 distributions [32], from [33].

[9]Because $v \ll 1$ the contribution $\propto G_2$ is very small also for unpolarized beams.

For $Q^2 \ll M_Z^2$ the terms $\propto G_2$ and H_2 are small corrections to F_2 only which allows to measure $F_2(x,Q^2)$ using (30). In figure 15 the expectation for a measurement of $F_2(x,Q^2)$ at HERA for $\sqrt{s}$ = 314 GeV, $x \geq 10^{-4}$, and $\mathcal{L} = 100pb^{-1}$ is shown referring to the parametrization of the quark distributions B_0 given in [32]. The parametrization B^- [32], assuming a rise of the gluon distribution as $\sim 1/\sqrt{x}$ for $x \to 0$, yields much higher values of F_2 and steeper slopes $\partial F_2/\partial Q^2$ in the small x range (figure 16).

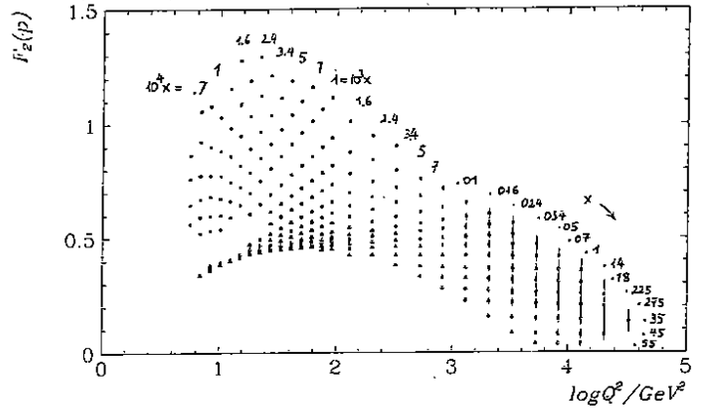

Figure 16: Statistical precision of $F_2(x,Q^2)$ for a measurement at HERA (E_e = 30 GeV and E_p = 820 GeV), $\mathcal{L} = 100pb^{-1}$, for KMRS-B^-, [33].

The effect of a low energy option at HERA E_e = 10 GeV and E_p = 300 GeV is shown in figure 17. At $Q^2 = const.$ the range of larger x values is filled because of the lower value of $\sqrt{s}$. This allows to measure the slope $\partial F_2/\partial Q^2$ in a much wider Q^2 range. Furthermore, F_2 is measuered at a higher statistics in the valence range also. This is very important for the QCD analysis as will be shown in section 8.

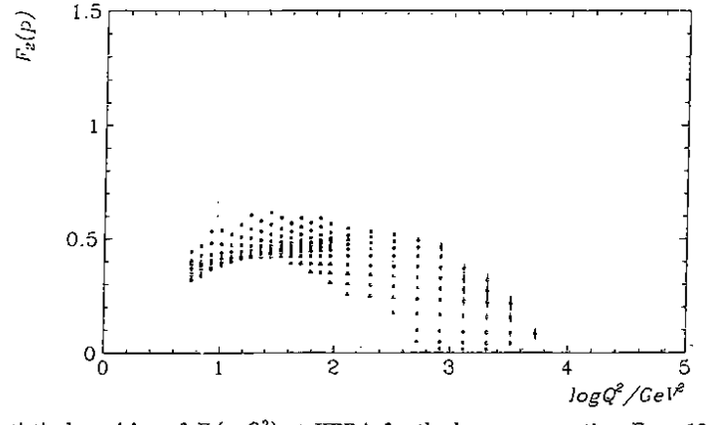

Figure 17: Statistical precision of $F_2(x,Q^2)$ at HERA for the low energy option E_e = 10 GeV and E_p = 300 GeV, $\mathcal{L} = 50pb^{-1}$, assuming the KMRS B^0 distributions, [33].

A later upgrade of HERA may allow to reach the energies $E_e = 45\,\mathrm{GeV}$ and $E_p = 1140\,\mathrm{GeV}$. In figure 18 the statistical precision of $F_2(x,Q^2)$ for a long-term run of $\mathcal{L} = 1 fb^{-1}$ at these beam energies is illustrated. The comparison with figure 16 shows that in the high Q^2 range the accuracy is improved.

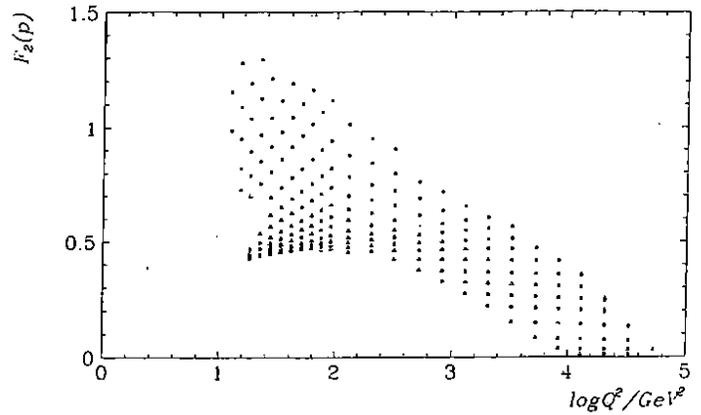

Figure 18: Statistical precision of $F_2(x,Q^2)$ at HERA for a later upgrade: $E_e = 45\,\mathrm{GeV}$ and $E_p = 1140\,\mathrm{GeV}$. Here, an integrated luminosity of $\mathcal{L} = 1 fb^{-1}$ was assumed and the parton parametrizations KMRS B^- were used, [33].

The measurement of $\hat{\sigma}^{e^\pm p}$ at LEP $\otimes$ LHC allows to approach the range of higher Q^2 and even smaller x. This is illustrated in figure 19 for one of the beam–energy options $\sqrt{s} = 1.3$ TeV. At large Q^2 the effect of Z–boson exchange is clearly visible.

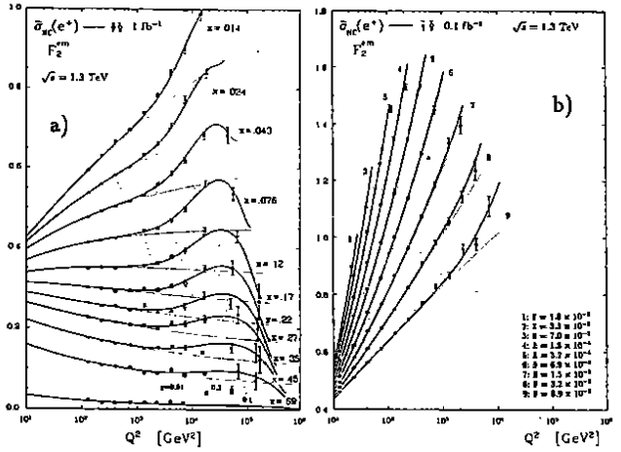

Figure 19: Q^2 dependence of $\tilde{\sigma}_{nc}(e^+) = xQ^4/(2\pi\alpha^2 Y_+)\hat{\sigma}^{e^+p}$ for (a) $x > 10^{-2}$ and (b) $10^{-5} < x < 10^{-2}$. The dots denote $\tilde{\sigma}_{nc}$ with statistical errors, referring to the parton parametrizations [35]. The dotted lines correspond to $F_2(x,Q^2)$, [12].

Similarly to (30), one may form the combination

$$\begin{aligned} B_-(\lambda) &= \frac{1}{2}\left[\hat{\sigma}^+_{nc}(-\lambda) - \hat{\sigma}^-_{nc}(+\lambda)\right] \frac{xQ^4}{2\pi\alpha^2} \frac{1}{Y_-(a-\lambda v)} \frac{1}{\kappa_Z} \\ &= xG_3 + [(\lambda(v^2+a^2) - 2va)/(a-\lambda v)]\kappa_Z x H_3 \end{aligned} \tag{31}$$

Again, the beam polarization λ in (31) may be tuned to eliminate the term $\propto H_3$. However, since $\kappa_Z \ll 1$, eq. (31) represents basically the structure function $xG_3(x,Q^2)$ already, which measures a combination of the valence quark densities (see (38)). It can be measured as a shape in x at high Q^2. This is illustrated in figure 20 for the kinematical conditions at HERA. Expectations for LEP $\otimes$ LHC are given in [36].

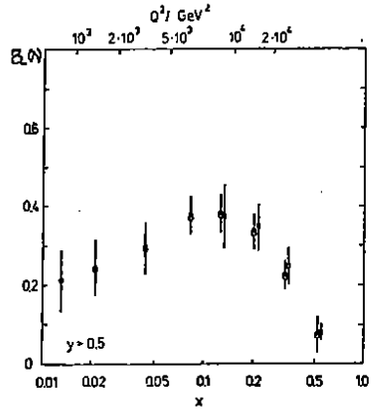

Figure 20: $B_-(\lambda)$ as a function of x for $Q^2 \gtrsim 500$ GeV^2. Full circles at $\sqrt{s} = 314\,\mathrm{GeV}$, $\lambda = 0$; open circles for $\lambda = 2va/(v^2+a^2)$; open squares: $\sqrt{s} = 110\,\mathrm{GeV}$, $\lambda = 0$ for $\mathcal{L} = 100 pb^{-1}$ per beam, [11].

Because the charged current cross sections in $l^\pm p$ scattering are determined by four structure functions their complete unfolding is not possible. However, one may approximately represent

$$W_2^{e^-p}(x,Q^2) \cong \frac{\hat{\sigma}^{e^-p}_{cc}}{[Y_+\kappa_W^2/2]} \frac{xQ^4}{2\pi\alpha^2} \tag{32}$$

which is illustrated in figure 21. Note, that the statistical errors are rather large under the conditions given at HERA. Eq. (32) is well fullfilled for small y, because there $Y_- xW_3(x,Q^2) \ll Y_+ W_2(x,Q^2)$.

A deuteron–option, similar to the case of $\nu(\overline{\nu})N$–scattering, otherwise, allows to measure the structure functions $W_2^{eN}(x,Q^2)$ and $xW_3^{eN}(x,Q^2)$[10]:

$$\begin{aligned} W_2^{eN}(x,Q^2) &= \frac{1}{Y_+\kappa_W^2} \frac{xQ^4}{2\pi\alpha^2} \left[\frac{\hat{\sigma}^{e^+d}_{cc}}{1+\lambda_+} + \frac{\hat{\sigma}^{e^-d}_{cc}}{1+\lambda_-}\right] \\ xW_3^{eN}(x,Q^2) &= \frac{1}{Y_-\kappa_W^2} \frac{xQ^4}{2\pi\alpha^2} \left[\frac{\hat{\sigma}^{e^+d}_{cc}}{1+\lambda_+} - \frac{\hat{\sigma}^{e^-d}_{cc}}{1+\lambda_-}\right] \end{aligned} \tag{33}$$

[10]Note, that the cms energy s is only half as large for $e^\pm d$ scattering compared to the case of $e^\pm p$ scattering.

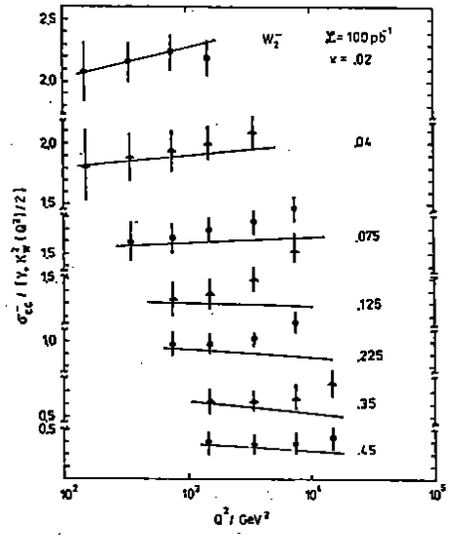

Figure 21: $100pb^{-1}$ measurement of $\hat{\sigma}^{e^-p}/(Y_+\kappa_W/2)$ yielding an approximate representation of $W_2^{e^-p}$ at small y ($\sqrt{s} = 314$ GeV), [11].

In figure 22 the statistcal accuracy for measurements of $W_2^{eN}(x,Q^2)$ at HERA and $xW_3^{eN}(x)$ at LEP $\otimes$ LHC are shown. Whereas W_2^{eN} can be measured as a two–dimensional quantity, for xW_3^{eN} only the shape in x may be determined, since xW_3 is measured as difference of two cross sections. However, due to the large cms energy at LEP $\otimes$ LHC values of x as small as 10^{-3} are reached.

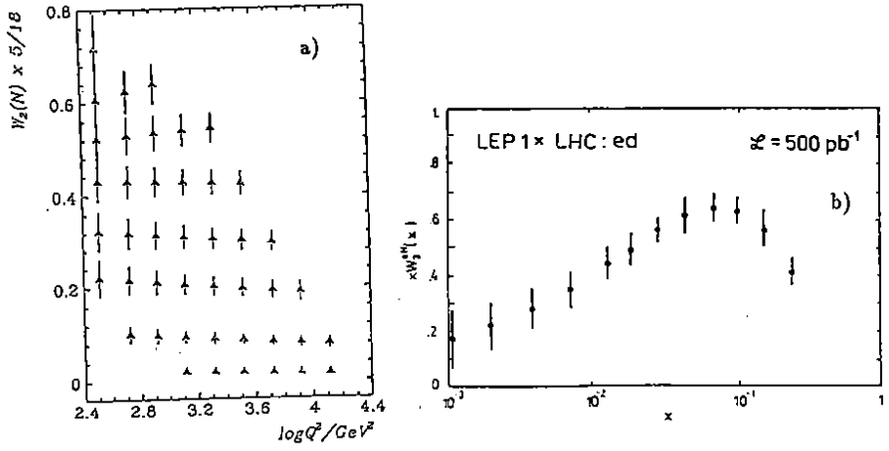

Figure 22: (a) Statistical precision of $(5/18)W_2^{eN}(x,Q^2)$ for a measurement at HERA with $\mathcal{L} = 100pb^{-1}$, $\sqrt{s} = 222$ GeV, [34], and (b) for $xW_3^{eN}(x)$ at LEP $\otimes$ LHC for $\mathcal{L} = 500pb^{-1}$, $\sqrt{s} = 894$ GeV, [36].

5.2 $\nu(\overline{\nu})N$

In the case of $\nu(\overline{\nu})p$ scattering at least four different structure functions contribute to the two measurable cross sections, and one can not unfold the structure structure functions without further assumptions. For isoscalar targets (e.g. deuterons, to keep nuclear effects as small as possible), however, one can determine the structure functions $\widehat{W}_2^d(x,Q^2)$ and $x\widehat{W}_3(x,Q^2)$ using

$$\begin{aligned}
\widehat{W}_2^d(x,Q^2) &= \frac{2\pi x}{G_F^2 Y_+}\frac{(M_W^2+Q^2)^2}{M_W^4}\left\{\hat{\sigma}_{cc}^{\nu N}+\hat{\sigma}_{cc}^{\overline{\nu}N}\right\} - \frac{2xY_-}{Y_+}(s(x,Q^2)+b(x,Q^2)-c(x,Q^2)) \\
x\widehat{W}_3^d(x,Q^2) &= \frac{2\pi x}{G_F^2 Y_+}\frac{(M_W^2+Q^2)^2}{M_W^4}\left\{\hat{\sigma}_{cc}^{\nu N}-\hat{\sigma}_{cc}^{\overline{\nu}N}\right\} \qquad (34)
\end{aligned}$$

These structure functions are averages of the corresponding structure functions describing either νd or $\overline{\nu}d$ interactions.

$$\begin{aligned}
\widehat{W}_2^d(x,Q^2) &= \frac{1}{2}\left[\widehat{W}_2^{\nu N}(x,Q^2)+\widehat{W}_2^{\overline{\nu}N}(x,Q^2)\right] \\
x\widehat{W}_3^d(x,Q^2) &= \frac{1}{2}\left[x\widehat{W}_3^{\nu N}(x,Q^2)+x\widehat{W}_3^{\overline{\nu}N}(x,Q^2)\right] \qquad (35)
\end{aligned}$$

While $x\widehat{W}_3^d(x,Q^2)$ can be measured directly from the cross sections $\widehat{W}_2^d(x,Q^2)$ requires to know the distribution $x(s+b-c)$, which can be inferred studying di–muon production. The expectations for the measurement of $\widehat{W}_2^d(x,Q^2)$ and $x\widehat{W}_3^d(x,Q^2)$ is illustrated in figure 23 assuming the experimental conditions described in section 3.

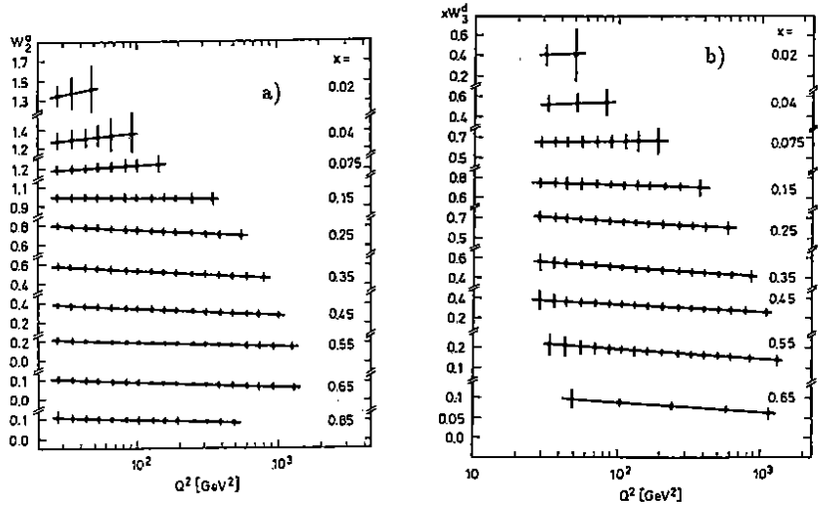

Figure 23: Statistical precision of charged current structure functions in a high energy neutrino experiment (see text). a) $\widehat{W}_2^d(x,Q^2)$; b) $x\widehat{W}_3^d(x,Q^2)$, [7].

One may try, in a similar way, to measure also neutral current νN structure functions. However, this requires to measure x and Q^2 with sufficient precision in this process. Contrary to $e^{\pm}N$ scattering the initial neutrino beam is not monochromatic, and both the variables x and

Q^2 have to be determined from the measurement of the current jet. In a fixed target experiment, however, this is extremely difficult even at high energies and only distributions in a single variable haven been measured so far [37].

6 Parton Model and Flavour Contents of Structure Functions

6.1 Representation of Structure Functions

In section 2 the hadronic tensor was expressed in terms of structure functions. In the kinematical range in which the deep inelastic scattering process may be described within the parton picture the structure functions can be written as linear combinations of parton densities. The parton picture assumes the validity of the factorization

$$\sigma_{B^*+N\to X}(x,Q^2) = \sum_q \int_0^1 dx_1 \int_0^1 dx_2 \delta(x - x_1 x_2) \sigma_{B^*+q\to q'}(x_1,Q^2) f_{q/N}(x_2,Q^2) \qquad (36)$$

where $\sigma_{B^*+N\to X}(x,Q^2)$ denotes the cross section for the scattering of the virtual boson B^* and the nucleon N, $\sigma_{B^*+q\to q'}(x_1,Q^2)$ the cross section for the hard subprocess, and $f_{q/N}(x,Q^2)$ is the number density associated with the parton q. Here, the factoriztion scale was choosen to be the virtuality Q^2. Corresponding relations may be given for higher order corrections in α_s or α also. In this way a straightforward calculation leads to the following expressions of the different neutral and charged current structure functions at the Born level.

For the case of $l^\pm N$ scattering one obtains

$$\begin{aligned} F_2(x,Q^2) &= x\sum_q e_q^2 \left[q(x,Q^2) + \overline{q}(x,Q^2)\right] \\ G_2(x,Q^2) &= x\sum_q 2e_q v_q \left[q(x,Q^2) + \overline{q}(x,Q^2)\right] \\ H_2(x,Q^2) &= x\sum_q (v_q^2 + a_q^2) \left[q(x,Q^2) + \overline{q}(x,Q^2)\right] \end{aligned} \qquad (37)$$

$$\begin{aligned} xG_3(x,Q^2) &= x\sum_q 2e_q a_q \left[q(x,Q^2) - \overline{q}(x,Q^2)\right] \\ xH_3(x,Q^2) &= x\sum_q 2v_q a_q \left[q(x,Q^2) - \overline{q}(x,Q^2)\right] \end{aligned} \qquad (38)$$

with

$$\begin{aligned} v_u &= +\frac{1}{2} - 2e_u \sin^2\theta_w & a_u &= +\frac{1}{2} \\ v_d &= -\frac{1}{2} - 2e_d \sin^2\theta_w & a_d &= -\frac{1}{2} \end{aligned} \qquad (39)$$

and

$$\begin{aligned} W_2^+(x,Q^2) &= 2x\sum_i \left[d_i(x,Q^2) + \overline{u}_i(x,Q^2)\right] \\ W_2^-(x,Q^2) &= 2x\sum_i \left[u_i(x,Q^2) + \overline{d}_i(x,Q^2)\right] \end{aligned} \qquad (40)$$

$$\begin{aligned} xW_3^+(x,Q^2) &= 2x\sum_i \left[u_i(x,Q^2) - \overline{d}_i(x,Q^2)\right] \\ xW_3^-(x,Q^2) &= 2x\sum_i \left[d_i(x,Q^2) - \overline{u}_i(x,Q^2)\right] \end{aligned} \qquad (41)$$

Here, we used the short–hand notation

$$\begin{aligned} u_i &= (u,c,t) \\ d_i &= (d,s,b)\,. \end{aligned} \qquad (42)$$

The neutrino neutral and charged current structure functions are represented by

$$\widehat{F}_2^\nu(x,Q^2) = 2x\left[a_{21}\sum_i (u_i + \overline{u}_i) + a_{22}\sum_i \left(d_i + \overline{d}_i\right)\right] \equiv \widehat{F}_2^{\overline{\nu}}(x,Q^2) \qquad (43)$$

$$x\widehat{F}_3^\nu(x,Q^2) = 2x\left[a_{31}\sum_i (u_i - \overline{u}_i) + a_{32}\sum_i \left(d_i - \overline{d}_i\right)\right] \equiv x\widehat{F}_3^{\overline{\nu}}(x,Q^2) \qquad (44)$$

where

$$\begin{aligned} a_{21} &= 1/4 - e_u \sin^2\theta_w + 2e_u^2 \sin^4\theta_w \\ a_{22} &= 1/4 + e_d \sin^2\theta_w + 2e_d^2 \sin^4\theta_w \\ a_{31} &= 1/4 - e_u \sin^2\theta_w \\ a_{32} &= 1/4 + e_d \sin^2\theta_w \end{aligned} \qquad (45)$$

and

$$\begin{aligned} \widehat{W}_2^{\nu p}(x,Q^2) &= 2x\sum_i \left[d_i(x,Q^2) + \overline{u}_i(x,Q^2)\right] \\ \widehat{W}_2^{\overline{\nu}p}(x,Q^2) &= 2x\sum_i \left[u_i(x,Q^2) + \overline{d}_i(x,Q^2)\right] \\ x\widehat{W}_3^{\nu p}(x,Q^2) &= 2x\sum_i \left[d_i(x,Q^2) - \overline{u}_i(x,Q^2)\right] \\ x\widehat{W}_3^{\overline{\nu}p}(x,Q^2) &= 2x\sum_i \left[u_i(x,Q^2) - \overline{d}_i(x,Q^2)\right] \end{aligned} \qquad (46)$$

6.2 Ways to unfold Parton Densities

6.2.1 $e^\pm N$ Scattering

The four independent cross sections $\hat{\sigma}_{nc}^+, \hat{\sigma}_{nc}^-, \hat{\sigma}_{cc}^+, \hat{\sigma}_{cc}^-$ measured in deep inelastic $e^\pm p$ scattering may be used to unfold four linear combinations of parton distributions. For the Born cross sections one obtains [11]:

$$\begin{pmatrix} U(x,Q^2) \\ \overline{U}(x,Q^2) \\ D(x,Q^2) \\ \overline{D}(x,Q^2) \end{pmatrix} = \left(\mathcal{A}_{ij}(x,Q^2)\right) \otimes \begin{pmatrix} \hat{\sigma}_{nc}^+ \\ \hat{\sigma}_{nc}^- \\ \hat{\sigma}_{cc}^+ \\ \hat{\sigma}_{cc}^- \end{pmatrix} \qquad (47)$$

where $U(\overline{U}) = x\sum_i u_i(\overline{u}_i)$ and $D(\overline{D}) = x\sum_i d_i(\overline{d}_i)$.

Before the unfolding (47) is possible the QED (section 4) and QCD corrections (section 7) have to be carried out for the differential cross sections. The QCD corrections include the complete F_L–terms which may become rather large for small values of x (cf. section 7). Furthermore,

depending on the size of the ratio m_Q^2/Q^2, part of the heavy flavour distributions may be considered as QCD correction, while another part is treated as part of the initial state at the given value of Q^2 [38].

Experimentally, eq. (47) requires, that the relative systematics of the positron and electron runs, as well as that of the neutral and charged current data samples, is well understood.

The mapping $(\mathcal{A}_{ij}(x,Q^2))$ is characterized by

$$\det_4\left(\mathcal{A}_{ij}(x,Q^2)\right) \sim \left\{\kappa_z(Q^2)\left[1-(1-y)^4\right]\right\}^{-1} \tag{48}$$

Thus, $(\mathcal{A}_{ij}(x,Q^2))$ becomes degenerate both for $Q^2 \ll M_Z^2$ and $y \ll 1$. As a result, the errors of $(U,\overline{U},D,\overline{D})$ become large in this range [11]. Since only at high Q^2 (see figure 6) the statistical errors of $\sigma_{cc}^{\pm}$ are of the same order as the errrors of $\sigma_{nc}^{\pm}$ the statistical precision of the unfolded distributions is almost determined by the errors of $\sigma_{cc}^{\pm}$.

Alternatively to (47) one may consider the mapping [11]

$$\begin{pmatrix} xu_v(x,Q^2) \\ xd_v(x,Q^2) \\ xs(x,Q^2) \end{pmatrix} = \left(\mathcal{B}_{ij}^{\pm}(x,Q^2)\right) \otimes \begin{pmatrix} \hat{\sigma}_{nc}^{\pm} \\ \hat{\sigma}_{cc}^{+} \\ \hat{\sigma}_{cc}^{-} \end{pmatrix} \tag{49}$$

assuming definite ratios for the sea quark distributions. For a luminosity of $\mathcal{L} = 100pb^{-1}$ per beam the accuracy obtainable for the x–shapes of the quark distributions is shown in figure 24.

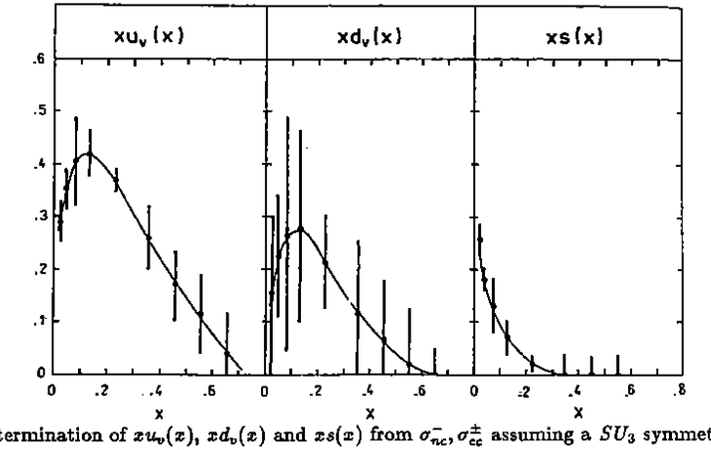

Figure 24: Determination of $xu_v(x)$, $xd_v(x)$ and $xs(x)$ from $\sigma_{nc}^{-}, \sigma_{cc}^{\pm}$ assuming a SU_3 symmetric sea[11] at $\sqrt{s} = 314$ GeV and $\mathcal{L} = 100pb^{-1}$ per beam, [11].

The unfolding of combinations of parton distributions was considered in [39, 40] for various cases. The total luminosity required in this study was $\mathcal{L} = 400\ pb^{-1}$ for the unfolding (47). As examples in figure 25 the precision of the x-shape of the distributions $U(x)$ and $F_s(x) \equiv \Sigma(x)$ are shown. In comparison with earlier measurements the range of higher Q^2 will be covered at HERA. Due to the small charged current statistics, however, two-dimensional dependences are not accessible.

In limited kinematical ranges combinations of cross sections, or some cross sections themselves, provide an approximate representation of parton distributions. In the valence range,

[11] Other ratios between sea quark distributions lead to similar results.

$x \gtrsim 0.25$, one finds for the charged current cross sections $\hat{\sigma}_{cc}^{\pm}$:

$$\begin{aligned} xu_v(x,Q^2) &= \frac{Q^4 x}{\pi\alpha^2}\frac{\hat{\sigma}_{cc}^{-}}{(Y_+ + Y_-)\,\kappa_W^2(Q^2)} \\ xd_v(x,Q^2) &= \frac{Q^4 x}{\pi\alpha^2}\frac{\hat{\sigma}_{cc}^{+}}{(Y_+ - Y_-)\,\kappa_W^2(Q^2)} \end{aligned} \tag{50}$$

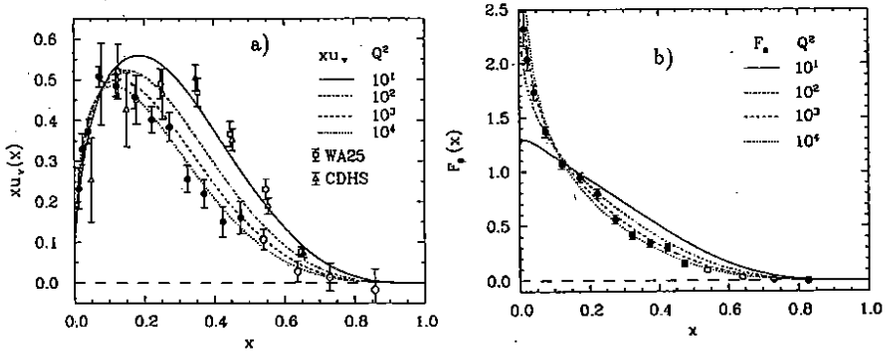

Figure 25: Extraction of (a) $xu_v(x)$ and (b) $F_s(x) \equiv \Sigma(x)$ from the NC and CC cross sections for e^-p and e^+p scattering using the ranges (a) $0.15 \le y \le 1$ and (b) $0.03 \le y \le 1$ for $\mathcal{L} = 400pb^{-1}$, [40].

The statistical precision obtained for $xu_v(x)$ and $xd_v(x)$ using (50) are depicted in figure 26.

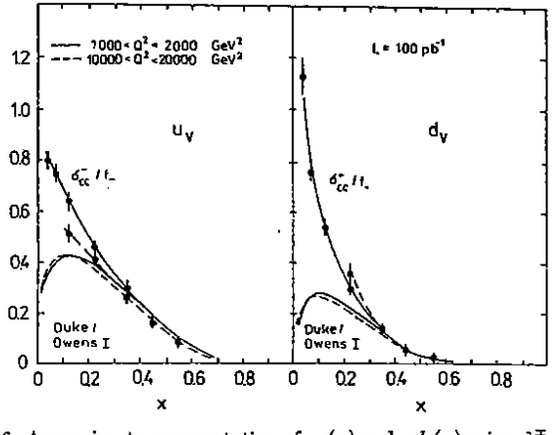

Figure 26: Approximate representation of $x_v(x)$ and $xd_v(x)$ using $\hat{\sigma}_{cc}^{\mp}$, [11].

More information on parton distributions may be extracted using also data on $e^{\pm}d$ scattering. In the valence range the structure functions $W_2^{eN}(x,Q^2)$ and $xW_3^{eN}(x,Q^2)$ are identical. Thus, the valence distribution $x(u_v + d_v)$ is measured best from W_2^{eN}. At smaller values of x the structure function xW_3^{eN} defines this distribution, however, with larger errors, since it is measured

by a difference of two cross sections. The antiquark distribution $x\overline{Q}(x,Q^2) = \sum_f x\bar{q}_f(x,Q^2)$ is given by

$$x\overline{Q}(x,Q^2) = \frac{1}{2}\left[W_2^{eN}(x,Q^2) - xW_3^{eN}(x,Q^2)\right] \tag{51}$$

Also, an inclusive measurement of the distribution $x(s-c)$ is possible via the combination [11]

$$x\left[s(x,Q^2) - c(x,Q^2)\right] = 3\left[\frac{5}{18}W_2^{eN}(x,Q^2) - F_2^{eN}(x,Q^2)\right] \tag{52}$$

Here, it was assumed, that the b-quark distribution can be safely neglected and $q_{s_i} \equiv \bar{q}_{s_i}$.

In figure 27 the x-shapes of the distributions $x\sum_i(q_i+\bar{q}_i)$, $x(u_v+d_v)$, $x\overline{Q}$ and $x(s-c)$ are illustrated for a possible measurement of the cross sections $\delta^{e^\pm N}_{cc,nc}$ for $\mathcal{L} = 50pb^{-1}$ per beam.

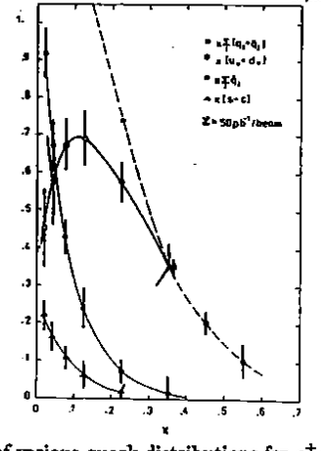

Figure 27: Statistical errors of various quark distributions for $e^\pm d$ runs and $\mathcal{L} = 50\ pb^{-1}$, [11].

6.2.2 νN Scattering

Single parton distributions may be measured also using deep inelastic charged current neutrino-nucleon scattering. Because the event samples contain a statistics of several 10^5 or 10^6 events (cf. sect. 3) a very precise measurement of the isolated parton distributions in x and Q^2 is possible. As shown in figure 23 already, the combinations $\Sigma(x,Q^2) \equiv \widehat{W}_2^d(x,Q^2)$ and $x[u_v(x,Q^2) + xd_v(x,Q^2)] \equiv x\widehat{W}_3^d(x,Q^2)$ can be measured very precisely. The combination

$$x[u_v(x,Q^2) - d_v(x,Q^2)] = \frac{4\pi x}{G_F^2}\frac{(M_W^2+Q^2)^2}{M_W^4}\frac{1}{Y_+ + Y_-}\left\{\frac{d^2\sigma^{\nu N}}{dxdQ^2} - \frac{d^2\sigma^{\nu p}}{dxdQ^2}\right\} \tag{53}$$

can be used together with (35 b) to determine $xu_v(x,Q^2)$ and $xd_v(x,Q^2)$. A possible measurement of $xu_v(x,Q^2)$ under the conditions lined out in section 3 is shown in Figure 28a. In the valence range, $xu_v(x,Q^2)$ and $xd_v(x,Q^2)$ can be measured from the $\nu(\overline{\nu})p$ cross sections directly:

$$\left.\begin{matrix} xu_v(x,Q^2) \\ xd_v(x,Q^2) \end{matrix}\right\} = \frac{2\pi x}{G_F^2}\frac{(M_W^2+Q^2)^2}{M_W^4}\frac{1}{Y_+ \mp Y_-}\left\{\begin{matrix} \frac{d^2\sigma^{\overline{\nu}p}}{dxdQ^2} \\ \frac{d^2\sigma^{\nu p}}{dxdQ^2} \end{matrix}\right. \tag{54}$$

The antiquark distribution $\sum_f x\bar{q}_f(x,Q^2)$ can be measured using

$$\begin{aligned}\sum_f x\bar{q}_f(x,Q^2) &= \frac{2\pi x}{G_F^2}\left(\frac{M_W^2+Q^2}{M_W^2}\right)^2\left[\frac{d^2\sigma^{\overline{\nu}d}}{dxdQ^2} - \frac{d^2\sigma^{\nu d}}{dxdQ^2}(1-y)^2\right]\frac{1}{Y_+Y_-} \\ &- \frac{Y_-}{Y_+}x\left[s(x,Q^2) + b(x,Q^2) - c(x,Q^2)\right]\end{aligned} \tag{55}$$

The statistical precision which may be obtained for this distribution is illustrated in Figure 28b. Compared with a corresponding measurement at HERA (cf. figure 27) the antiquark distribution can be measured both in x and Q^2.

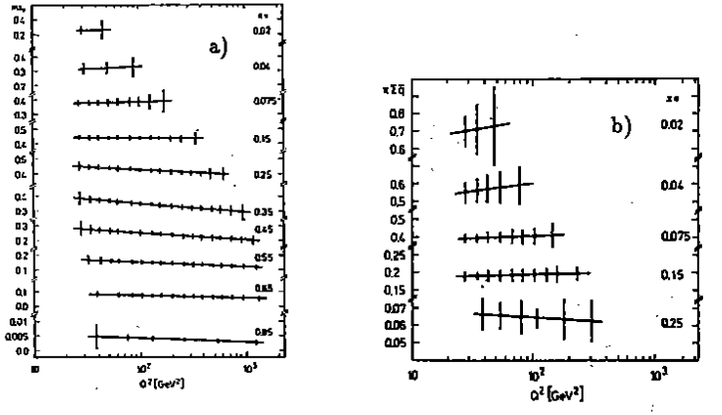

Figure 28: Statistical precision of the measurement of (a) $xu_v(x,Q^2)$ and (b) $\sum_f \bar{q}_f(x,Q^2)$ in a neutrino experiment (see text), from [7].

6.2.3 Heavy Flavours

So far, all flavours have been delt with as effectively 'massless' in the representation of structure functions in section 6.1,6.2. Indeed, if $W^2 \gg m_q^2$, this is a sufficient approximation. However, in the threshold range, the Q^2 behaviour of the heavy flavour distributions is effected not only by the logarithmic scaling violations but also by $(m_q^2/Q^2)^n$ terms. Furthermore, these effects depend on the type of the intermediary boson through which the deep inelastic process proceeds.

In a good approximation the heavy quark distributions of nucleons may be described by the Bethe–Heitler process of boson (γ, Z, $W^\pm$)–gluon fusion:

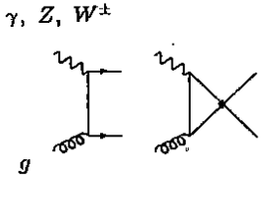

Figure 29: Lowest order α_s contribution to heavy quark pair-production: B-g-fusion.

The cross section for $Q'\overline{Q}$ production was investigated for neutral and charged current deep processes by many authors [41, 42]. For the example of $\gamma^* g$ fusion one obtains the following contributions to $F_2(x,Q^2)$ and $F_L(x,Q^2)$:

$$F_{2,L}^{Q\overline{Q}}(x,Q^2) = \frac{\alpha_s(Q^2)}{\pi} e_Q^2 \int_0^1 \frac{dy}{y} y G(y,Q^2) f_{2,L}^{\gamma^* g \to Q\overline{Q}}\left(\frac{x}{y},Q^2\right) \theta(z-ax) \tag{56}$$

with

$$\begin{aligned} f_2^{\gamma^* g \to Q\overline{Q}}(z,Q^2) &= v\left[4z^2(1-z) - \frac{z}{2} - \frac{2m_Q^2}{Q^2} z^2(1-z)\right] \\ &+ \left[\frac{z}{2} - z^2(1-z) + \frac{2m_Q^2}{Q^2} z^2(1-3z) - \frac{4m_Q^4}{Q^4} z^3\right] \ln\frac{1+v}{1-v} \\ f_L^{\gamma^* g \to Q\overline{Q}}(z,Q^2) &= 2z^2(1-z)v - \frac{4m_Q^2}{Q^2} \ln\frac{1+v}{1-v} \end{aligned} \tag{57}$$

with $a = 1 + 4m_Q^2/Q^2$ and $v = 1 - (4m_Q^2/Q^2)z/(1-z)$. In the massless limit $f_L^{\gamma^* g \to Q\overline{Q}}(z,Q^2)$ approaches the splitting function (60), whereas $f_2^{\gamma^* g \to Q\overline{Q}}(z,Q^2)$ exhibits a logarithmically singular term. In the limit $m_Q^2/Q^2 \to 0$ the heavy flavour Q becomes light, and one has to sum these terms in all orders, i.e. absorb the mass singularity into the scaling violations of the 'massless' part of $F_2^{Q\overline{Q}}(x,Q^2)$. Thus, rather than using (57) one may define

$$F_2^{Q\overline{Q}}(x,Q^2) = F_{2,0}^{Q\overline{Q}}(x,Q^2) + \frac{\alpha_s(Q^2)}{\pi} e_Q^2 \int_0^1 \frac{dy}{y} y G(y,Q^2) \bar{f}_2^{\gamma^* g \to Q\overline{Q}}\left(\frac{x}{y},Q^2\right) \theta(z-ax) \tag{58}$$

with

$$\bar{f}_2^{\gamma^* g \to Q\overline{Q}}(z,Q^2) = f_2^{\gamma^* g \to Q\overline{Q}}(z,Q^2) - \frac{z}{2}\left[z^2 + (1-z)^2\right] \ln\left(\frac{W^2}{m_Q^2}\right) \tag{59}$$

and $F_{2,0}^{Q\overline{Q}}(x,Q^2)$ being the contribution to $F_2^{Q\overline{Q}}$ in the massless limit. Eq. (58) provides a smooth interpolation between the massless and massive case. Of course, the subtraction of the logarithmic mass–singularity is not unique because the constant terms depend on the factorization scheme in finite order, which one may choose differently (see e.g. [43]). The subtracted term in (59) contains the splitting function $P_{qg}(z)$ and the factorization scale W^2, emerging naturally if the mass singularity is regulated introducing a finite quark mass (cf. e.g. [44], eq. A.6).

6.3 Parametrization of Parton Distributions

In early attempts only the x–shape of the quark and gluon distributions have been estimated by comparison to data, mainly in the range of low Q^2 [45]. Later, the QCD evolution equations (see section 8) have been solved using an ansatz for the different parton densities at a scale Q_0^2 accounting for the Q^2 behaviour of the nucleon structure functions. The pioneering work by Buras and Gaemers [46] was followed by the analysis of deep inelastic scattering data and data from other hard processes (Drell–Yan process, high–p_T photoproduction, jet–, J/ψ– and W,Z–production) by different groups during the last decade [47]. For the numerical solution of the evolution equations different algorithms were developed [48] based on the inversion of Mellin moments, orthogonal polynomial expansions, and direct numerical solutions. Several of these methods have been compared (see e.g. [49]) and found to agree rather well. The most

recent parametrizations, based on the currently most precise data on hard processes and QCD evolution equations in next to leading order are [50]–[52].

With the advent of new data in the small x and high Q^2 or p_T^2 range these parametrizations will be further improved[12]. Currently also dynamical terms are included into the evolution equations which become relevant in the range of small x.

In figure 30 the parton distributions of two recent fits (CTEQ1M [51] and D_0' [52]) are compared.

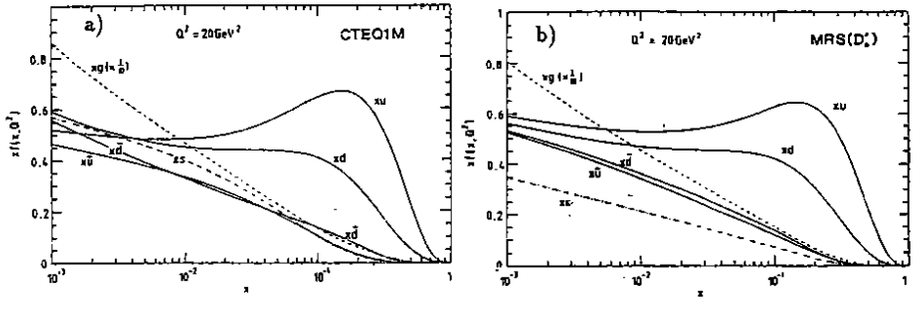

Figure 30: The parton distributions of the proton at $Q^2 = 20\,\mathrm{GeV}^2$ corresponding to (a) set CTEQ1M and to (b) D_0' of MRS [52] of [51]; from [54].

Whereas in the range of larger values of x these parametrizations do widely agree, they deviate at small x for the sea quark distributions. Especially the strange quark distribution comes out be even larger than the $\overline{u}$ and $\overline{d}$ quark distribution in [51]. Currently, different results are obtained for the strange quark distribution using di–muon data or deriving the distribution $xs(x,Q^2)$ from eq. (52), combining data from the NMC and CCFR experiments. The current differences between the parton distributions obtained by different groups require further analyses to obtain a unique representation.

7 Access to the Gluon Distribution

In lowest order no diagrams contribute to the different deep inelastic scattering cross sections containing initial state gluons since the electro–weak gauge bosons are colour neutral. Thus, contributions $\propto xG(x,Q^2)$ emerge only with $\mathcal{O}(\alpha_s)$. In the range of small x $\alpha_s(Q^2)xG(x,Q^2)$ is large and the gluon distribution $xG(x,Q^2)$ can be extracted from deep inelastic scattering data using the measurement of $F_L(x,Q^2)$, heavy flavour ($Q = c,b$) pair production, and the J/ψ or Υ production cross sections. Furthermore, the gluon distribution $xG(x,Q_0^2)$ can be determined from the scaling violations of structure functions. This will be discussed separately in section 8.4.

[12] A program library containing the actual and earlier parametrizations of parton distributions was created by H. Plothow–Besch [53].

7.1 F_L

The differential cross sections (3) are determined by three structure functions in general. The combination $B_+(\lambda)$ eq. (30) can be utilized to eliminate the $\mathcal{F}_3$ (or W_3) terms. The remaining contributions $\mathcal{F}_{2,L}$ ($W_{2,L}$) may be disentangled varying y at *fixed* x and Q^2. This is achieved by using data taken at different $\sqrt{s}$. The measurement of F_L is only possible in the overlap–ranges of the respective kinematical domains corresponding to the different cms energies (see e.g. figure 4,5).

In leading order in α_s the longitudinal structure function $F_L(x,Q^2)$ is related to the parton densities by [55]

$$F_L(x,Q^2) = \frac{\alpha_s(Q^2)}{2\pi}\left\{C_q(\gamma^*)\int_x^1 \frac{dy}{y}\left(\frac{x}{y}\right)^2 F_2(y,Q^2) + C_g(\gamma^*)\int_x^1 \frac{dy}{y}\left(\frac{x}{y}\right)^2\left(1-\frac{x}{y}\right) yG(y,Q^2)\right\} \tag{60}$$

for photon exchange. Here, $C_q(\gamma^*) = 8/3$ and $C_g(\gamma^*) = 2\sum_{q,\overline{q}} e_q^2$. The diagrams contributing to (60) and the corresponding expressions of the longitudinal structure functions for the other processes are shown in figure 31.

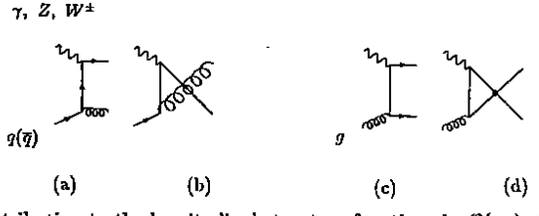

Figure 31: Diagrams contributing to the longitudinal structure functions in $\mathcal{O}(\alpha_s)$. The diagrams (c) and (d) describe the lowest order contributions to heavy quark pair–production (section 7.2) as well.

The longitudinal structure functions associated with the other differential cross sections can be constructed from

$$q_L(x,Q^2) = \frac{\alpha_s(Q^2)}{\pi}\left\{C_F\int_x^1 \frac{dy}{y}\left(\frac{x}{y}\right)^2 y[q(y,Q^2)+\overline{q}(y,Q^2)] + 2\int_x^1 \frac{dy}{y}\left(\frac{x}{y}\right)^2\left(1-\frac{x}{y}\right) yG(y,Q^2)\right\} \tag{61}$$

One has then to form the according linear combinations using (61) similarly to the combination of e.g. $G_2(x,Q^2) = \sum_q 2e_q v_q x[q(x,Q^2)+\overline{q}(x,Q^2)]$, i.e. $G_L(x,Q^2) = \sum_q 2e_q v_q q_L(x,Q^2)$ etc.

The statistical precision of the measurements of F_L has been estimated for HERA [11, 56, 57], LEP ⊗ LHC [36], and the neutrino experiment [7]. In figure 32 the expectations for $R = F_L/2xF_1$ ($F_2 = F_L + 2xF_1$) are shown for the case of the HERA experiments and the high energy neutrino experiment. In the former case $R(x)$ can be measured very precisely at small $x \sim 10^{-3}$, while in the latter case $R(x)$ can be well measured in the range of $\mathcal{O}(x \sim 0.1)$. In the case of the neutrino experiment the variation of y at fixed x and Q^2 is obtained naturally due to the ν and $\overline{\nu}$ beam spectra (see figure 2). At LEP ⊗ LHC a precise determination of $R(x)$ will even be possible down to $x \simeq 10^{-5}$ [36].

For $x \ll 1$ one can solve (60) for $xG(x,Q^2)$ approximately [56].

$$xG(x,Q^2) \simeq \frac{3}{5}5.85\left\{\frac{3\pi}{4\alpha_s(Q^2)}F_L(0.4x,Q^2) - \frac{1}{2}F_2(0.8x,Q^2)\right\} \tag{62}$$

A combined measurement of $F_L(x,Q^2)$ and $F_2(x,Q^2)$ at different values of x can thus be used to reconstruct $xG(x,Q^2)$ directly. This has been studied for the case of HERA in [56, 57] and for LEP ⊗ LHC in [36]. The statistical precision which may be obtained for this measurement of the gluon distribution is depicted in figure 33.

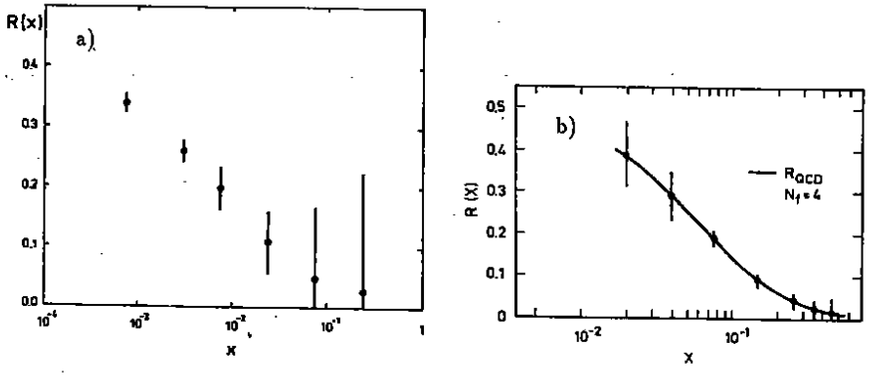

Figure 32: (a) Possible measurement of $R(x)$ for two energies $\sqrt{s} = 190, 314\,\text{GeV}$, $\mathcal{L} = 100pb^{-1}$ each, and averaged over Q^2, [11]; (b) possible measurement of $R(x)$ for the neutrino experiment using νd and $\overline{\nu}d$ data, [7].

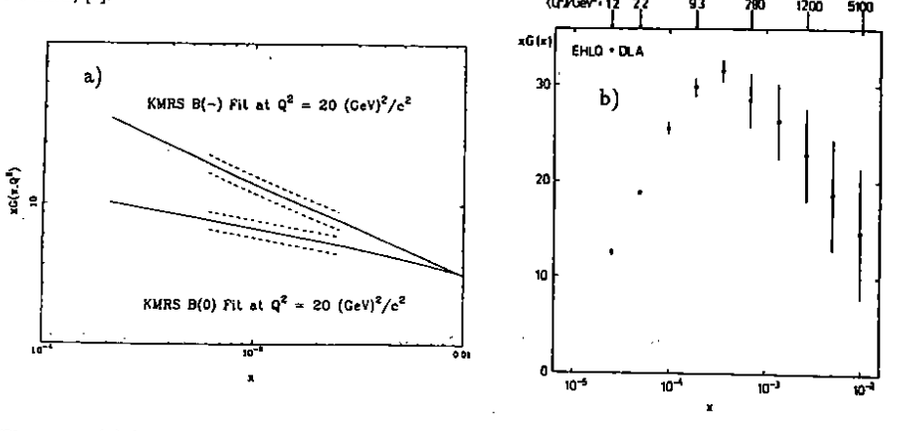

Figure 33: (a) Gluon distribution at low x and measureable domain with errors at HERA, [57]; (b) statistical precision of a possible measurement of $xG(x)$ at LEP ⊗ LHC using (62). Here, F_L was determined in the overlap range of a combined measurement at $\sqrt{s} = 1265\,\text{GeV}$, $\mathcal{L} = 1fb^{-1}$, and $\sqrt{s} = 1789\,\text{GeV}$, $\mathcal{L} = 100pb^{-1}$, and the average over Q^2 was taken, from [36].

At HERA (62) can be used to measure $xG(x)$ in the range $6\cdot10^{-4} \lesssim x \lesssim 3\cdot10^{-3}$ with a sufficient precision to distinguish between the case $xG(x,Q_0^2) \to const.$ or $\propto 1/\sqrt{x}$. At LEP ⊗ LHC above $x \sim 3\cdot10^{-4}$ only the shape of $xG(x)$ averaged over Q^2 can be determined. At lower x the statistical error of F_L is much smaller and one can determine the behaviour of $xG(x,Q^2)$ even

in a few bins in Q^2 at $x = const.$

Earlier calculations of $F_L(x,Q^2)$ in $\mathcal{O}(\alpha_s^2)$ [58] have been checked and corrected recently [59]. The results found in ref. [59] for F_L in x–space agree completely with an independent calculation based on moments [60], as was shown by a numerical comparison. The second order corrections turn out to be very large, and may reach -25 % to -40 % at $x \sim 10^{-4}$ for typical values of $Q^2 \sim 10\,\mathrm{GeV}^2$. This is illustrated in figure 34.

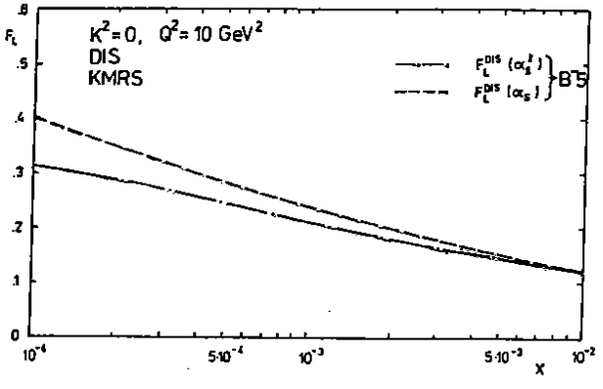

Figure 34: Comparison of 1st and 2nd order contributions to $F_L(x,Q^2)$ [59] for $Q^2 = 10\,\mathrm{GeV}^2$ using the parton distributions KMRS B^- [32].

Besides of the contributions to $F_L(x,Q^2)$ in $\mathcal{O}(\alpha_s^2)$ new terms emerge in the small–x range due to the fact, that the transverse momentum of the gluon can not be neglected in general [61]. Due to these contributions other terms modifying eq. (62), which was derived assuming (60), arise.

7.2 $\sigma_{Q\overline{Q}}$

As a second method the measurement of the heavy flavour pair production cross section $\sigma(e^\pm p \to Q\overline{Q}X)$ can be used to determine the gluon distribution [62]-[64]. In lowest order only the diagrams of figure 31 c and d contribute. In the case of charm production the cross section can either be measured tagging $D^{*\pm}$ mesons via $D^{*\pm} \to D^0\pi^\pm \to (K^\mp\pi^\pm)\pi^\pm$ or the measurement of inclusive dileptons from $c\bar{c} \to l^+l^-X$. For D^* production the longitudinal momentum fraction of the proton carried by the gluon, x_g, can be reconstructed using

$$x_g = \frac{\hat{s} + Q^2 + K^2}{ys} \simeq \frac{\hat{s}}{ys} \tag{63}$$

for both $Q^2, K^2 \ll \hat{s}$, with k the gluon momentum, $K^2 = -k^2$, $\hat{s} \simeq (p_\perp^2(D^*) + m_c^2)/z(1-z)$, and $z = P.p_c/[y(P.l_e)]$.

In the case of inclusive dilepton events x_g can be measured from the rapidity of the $c\bar{c}$–system, $\hat{y}_{c\bar{c}}$, assuming quasi–collinear γg–collisions:

$$x_g = \frac{yE_e}{E_p}\exp(2\hat{y}_{c\bar{c}}) \tag{64}$$

The statistical precision which may be obtained for the reconstruction of the gluon distribution using $D^{*\pm}$ tagging or the measurement of dileptons is shown in figure 35 for the conditions

at HERA. As in the case of F_L one can distinguish the cases of a rising ($\propto 1/\sqrt{x}$) or a flat gluon density in the small x range. Note however, that an uncertainty of the choice of the factorization scale exists. For the lowest order process this effect is illustrated in figure 35 b varying μ^2 within a factor of four. Similar results were obtained in a study for LEP $\otimes$ LHC [64] where the accessible kinematical range is extended to $x \sim 10^{-4}$. For the experimental determination of the gluon density it is important to eliminate resolved photon contributions [65] to the $Q\overline{Q}$–production cross section. This can be achieved selecting truely deep inelastic events via the Q^2 measurement using the scattered electron.

The $\mathcal{O}(\alpha_s)$ corrections to heavy flavour pair production were calculated in [66]. The K–factors for both the structure functions $F_{2,L}(x,Q^2,m_c^2)$ are rather large. In the range $10^{-4} < x < 10^{-1}$ they vary in the range between 1 and 2.5 depending on the choice of the factorization mass $\mu \in [M/2, 2M]$ with $M = \sqrt{Q^2 + 4m_c^2}$ and $m_c = 1.5\,\mathrm{GeV}$. Furthermore, in the range of small–x new dynamical effects due to the Lipatov equation [67] contribute. These effects have been studied in [68].

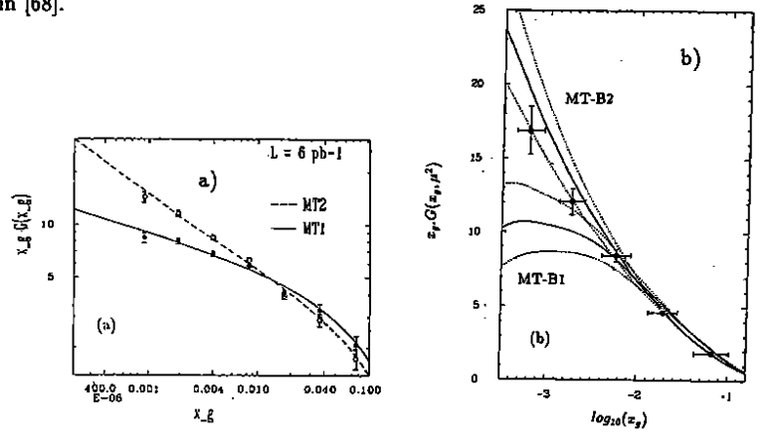

Figure 35: Reconstructed gluon densities (a) from inclusive $D^{*\pm}$ production using the gluon distributions by Morfin and Tung [47] for $\mathcal{L} = 6pb^{-1}$; (b) from dileptonic tagged charm events choosing $\mu^2 = \langle\hat{s}\rangle(x_g)$. The lower (upper) dotted curves correspond to the choice of the factorization scale $\mu^2/2$ · $(2\mu^2)$, [63].

7.3 $\sigma_{J/\psi}$

The deep inelastic production of J/ψ mesons in neutral current $e^\pm$ reactions [69] is a third method to measure the gluon density [70, 71, 64]. In this process the factorization scale μ^2 is effectively of the order of $m_{J/\psi}^2$ and thus much smaller than choosen in the other cases discussed already.

J/ψ mesons can be produced by various mechanisms in neutral current reactions at $e^\pm p$ colliders. Aside inelastic production $\gamma^* + g \to J/\psi + g$ described by the colour–singlet (CS) model [69] (see figure 36) further *(i)* inelastic and *(ii)* elastic production channels contribute. Inelastic channels are photoproduction $P + \gamma \to J/\psi + X$ and diffractive pomeron–photon ($\mathbf{P}\gamma$) fusion, i.e. $P + \gamma \to X + (\gamma + \mathbf{P}) \hookrightarrow J/\psi$. The elastic channels are: photon–pomeron fusion $\gamma + \mathbf{P} \to J/\psi$, $\gamma + \mathbf{P} \hookrightarrow (g \hookrightarrow c\bar{c})g \to J/\psi$, and $\gamma + \mathbf{P} \to J/\psi + X$, $\mathbf{P}^* \to X + g^*$ with subsequent

$g\gamma$-fusion in the CS-model. Furthermore, resolved photon processes, photon-photon fusion, b decays, and double charm production $(\gamma, g) + g \to J/\psi + c\bar{c}$ contribute.

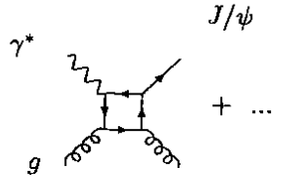

Figure 36: Diagram for the process $\gamma^* + g \to J/\psi + X$. In lowest order five other diagrams contribute.

The different background processes can be suppressed choosing suitable kinematical cuts. In the case of HERA these cuts are [71]: $z = (P.p_{J/\psi})/(P.q) < 0.9$, $p_\perp^{J/\psi} > 1\,\mathrm{GeV}$, and $p_X^2 > 10\,\mathrm{GeV}^2$.

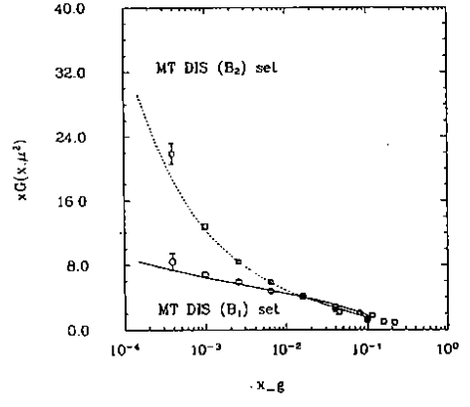

Figure 37: The gluon density reconstructed from inelastic J/ψ production in the kinematical range at HERA using the Morfin-Tung parametrization [47] as the input. The statistical errors correspond to $\mathcal{L} = 50pb^{-1}$ for MT-B1 and $\mathcal{L} = 20pb^{-1}$ for MT-B2. The curves show the used input densities $xG(x, \mu^2 = \langle\hat{s}\rangle)$, [71].

Under these conditions one may estimate the statistical precision with which the gluon distribution can be measured. The result of a recent analysis [71] is shown in figure 37. Corresponding results for the case of LEP $\otimes$ LHC have been given in [64].

The K-factor for deep inelastic J/ψ electroproduction is expected to be large since $\mu^2 \simeq m_{J/\psi}^2$ is rather small. J/ψ mesons can be treated as S-wave bound states of the $c\bar{c}$ system. The production cross section depends thus on the wave function at the origin $|\psi(0)|^2$ if bound state effects are neglected[13]. Usually, $|\psi(0)|^2$ is measured from the partial decay width $\Gamma_{l\bar{l}}$, for which the $\mathcal{O}(\alpha_s)$ correction [73]

$$\Gamma_{l\bar{l}} = \Gamma_{l\bar{l}}^0 \left(1 - \frac{16}{3}\frac{\alpha_s}{\pi}\right) \tag{65}$$

yields already a factor ~ 2. The complete $\mathcal{O}(\alpha_s)$ corrections are currently calculated [74].

[13]Relativistic corrections to the CS model have been calculated in [72].

8 QCD Tests: α_s, Λ_{QCD} and the Gluon Density

The scaling violations of the structure functions measured so far have been found to be in accord with the prediction of the QCD evolution equations in next-to-leading order in the range $x \gtrsim 0.005$ and $Q^2 \gtrsim 4\,\mathrm{GeV}^2$. This is even more remarkable as the corresponding evolution equations (Gribov-Lipatov-Altarelli-Parisi (GLAP) equations [75]) were derived for moderate x values only, assuming strong ordering for the transverse momenta.

To formulate the evolution equations we introduce singlet and non-singlet combinations of quark densities.

$$\Delta_{ij}^{NS}(x, Q^2) = q_i(x, Q^2) - \bar{q}_j(x, Q^2), \quad i, j \text{ arbitrary} \tag{66}$$

$$\Sigma(x, Q^2) = \sum_{i=1}^{N_f} \left[q_i(x, Q^2) + \bar{q}_i(x, Q^2)\right] \tag{67}$$

Here, N_f denotes the number of 'active' quark families, i.e. which may be produced at the values of x and Q^2 given. For neutral current interactions a respective condition reads $W^2 = Q^2(1-x)/x \geq 4m_q^2$.

Let us first consider the non-singlet evolution in leading order. The evolution equation may be derived similarly to the case of the QED radiative corrections discussed in section 3. The process of single gluon emission from a quark line is described by

$$dq_{NS}(x, k^2) = \frac{1}{8\pi^2} g_s^2(k^2) P_{NS}(x) \frac{dk^2}{k^2} \otimes q_{NS}(x, k^2) \tag{68}$$

Here, $g_s(k^2) = \sqrt{4\pi\alpha_s(k^2)}$ denotes the strong coupling constant. In leading order $\alpha_s(Q^2)$ is given by

$$\alpha_s^{LO}(Q^2) = \frac{4\pi}{\beta_0} \frac{1}{\log(Q^2/\Lambda^2)} \tag{69}$$

with $\beta_0 = (11/3)C_G - (4/3)T_R N_f$, $C_G = 3$, and $T_R = 1/2$. The convolution ($\otimes$) is defined by

$$A(x) \otimes B(x) = \int_0^1 dx_1 \int_0^1 dx_2 \delta(x - x_1 x_2) A(x_1) B(x_2). \tag{70}$$

One finds

$$P_{NS}(x) = C_F \left[\frac{1 - x^2}{(1-x)_+} + \frac{3}{2}\delta(1-x)\right] \tag{71}$$

and

$$\int_0^1 dx \varphi(x) [F(x)]_+ = \int_0^1 dx [\varphi(x) - \varphi(1)] F(x). \tag{72}$$

for the distribution $[F(x)]_+$. $\varphi(x)$ denotes a test function $\epsilon\ \mathcal{D}^\infty[0, 1]$. During the evolution from Q_0^2 to Q^2 the quark line emits gluons successively. Let us denote the sequential momenta along the quark line with k_i. In the Sudakov representation they are

$$k_i = \alpha_i q' + \beta_i P + k_{i\perp} \tag{73}$$

with $q' = q + xP$, $q'.k_{i\perp} = P.k_{i\perp} = 0$, and $q'^2 = P^2 = 0$.

To derive the evolution equations in LLA the integration over the transverse ($k_{i\perp}$) and longitudinal (β_i) variables can be done separately. For the transverse momenta only the ranges

$$Q_0^2 \ll k_{1\perp}^2 \ll k_{2\perp}^2 \ldots \ll k_{N\perp}^2 \ll Q^2 \tag{74}$$

contribute iterating (68) to infinite order. One obtains

$$\int_{Q_0^2}^{Q^2}\frac{dk_1^2}{2k_1^2}g^2(k_1^2)\int_{Q_0^2}^{k_1^2}\frac{dk_2^2}{2k_2^2}g^2(k_2^2)...\int_{Q_0^2}^{k_{N-1}^2}\frac{dk_N^2}{2k_N^2}g^2(k_N^2)\approx\frac{1}{N!}\left\{\frac{1}{2\pi\beta_0}\ln\left[\frac{\ln(Q^2/\Lambda^2)}{\ln(Q_0^2/\Lambda^2)}\right]\right\}^N \tag{75}$$

For the iteration in the longitudinal variables one obtains

$$J_L^{(N)}(x)=\otimes_{i=1}^N P_{NS}(x). \tag{76}$$

The β_i obey $1\geq\beta_1\geq\beta_2\geq...\geq\beta_n\geq x$ and the radiation is dominantly along the direction of P.

The *n-th* Mellin moment of (76) is

$$\int_0^1 dx x^{n-1}J_L^{(N)}(x)=\left[\int_0^1 dz z^{n-1}P_{NS}(z)\right]^N=\left[-\frac{\gamma_{NS}^{(0,n)}}{4}\right]^N \tag{77}$$

$\gamma_{NS}^{(0,n)}$ denotes the NS–anomalous dimension[14]

$$\gamma_{NS}^{(0,n)}=4C_F\left[\frac{1}{2}-\frac{1}{n(n+1)}+2\sum_{j=2}^n\frac{1}{j}\right]. \tag{78}$$

Here we used the property of (70)

$$M_n\{A(x)\otimes B(x)\}=M_n\{A(x)\}\cdot M_n\{B(x)\}. \tag{79}$$

Thus, the complete moment reads

$$\begin{aligned}M^{(n)}(Q^2) &= M^{(n)}(Q_0^2)\sum_{N=0}^\infty\frac{1}{N!}\left\{-\frac{\gamma_{NS}^{(0,n)}}{8\pi\beta_0}\ln\left[\frac{\ln(Q^2/\Lambda^2)}{\ln(Q_0^2/\Lambda^2)}\right]\right\}^N\\ &= M^{(n)}(Q_0^2)\exp\left\{-\frac{\gamma_{NS}^{(0,n)}}{8\pi\beta_0}\ln\left[\frac{\ln(Q^2/\Lambda^2)}{\ln(Q_0^2/\Lambda^2)}\right]\right\}.\end{aligned} \tag{80}$$

Eq. (80) is a solution of the partial differential equation

$$\frac{\partial M^{(n)}(Q^2)}{\partial\ln Q^2}=-\frac{\alpha_s(Q^2)}{8\pi}\gamma_{NS}^{(0,n)}M^{(n)}(Q^2). \tag{81}$$

Finally, the inverse Mellin transformation of (81) yields

$$\frac{\partial q_{NS}(x,Q^2)}{\partial\ln Q^2}=\frac{\alpha_s(Q^2)}{2\pi}P_{NS}(x)\otimes q(x,Q^2). \tag{82}$$

[14]Eq. (78) may be derived by direct integration using (71,77):

$$\int_0^1 dz\left[\frac{3}{2}\delta(1-z)+\frac{(1+z^2)}{(1-z)_+}\right]z^{(n-1)}=\frac{3}{2}-2\sum_{j=0}^{n-2}\frac{1}{j+1}-\frac{2n+1}{n(n+1)}\equiv-\gamma_{NS}^{(0,n)}/4C_F.$$

This illustrates the 'marriage' [76] of the intuitive approach [75] based on the Weizsäcker–Williams approximation and the formal approach [77] using the operator product expansion [78] in which the anomalous dimensions have been calculated first.

The non–singlet evolution equation (82) may be also written in terms of an evolution operator E_{NS}:

$$q_{NS}(x,Q^2)=E_{NS}(x,Q^2,Q_0^2,\Lambda)\otimes q_{NS}(x,Q_0^2) \tag{83}$$

which itself obeys the evolution equation

$$\frac{\partial E_{NS}(x,Q^2,Q_0^2,\Lambda)}{\partial\ln Q^2}=\frac{\alpha_s(Q^2)}{2\pi}C_F P_{NS}(x)\otimes E_{NS}(x,Q^2,Q_0^2,\Lambda) \tag{84}$$

with the initial condition

$$E_{NS}(x,Q^2=Q_0^2)=\delta(1-x). \tag{85}$$

Thus, (84) is fully determined by perturbative QCD, while (83) contains the *non–perturbative* input–density $q_{NS}(x,Q_0^2)$ also. Equations of the type (84) allow a clear separation of the perturbative and the non perturbartive contributions. While the former terms can be calculated within QCD the latter need to be determined by data.

For the singlet and gluon diensities a similar evolution equation is obtained. In matrix form it reads

$$\frac{\partial}{\partial\ln Q^2}\begin{pmatrix}\Sigma(x,Q^2)\\ xG(x,Q^2)\end{pmatrix}=\frac{\alpha_s(Q^2)}{2\pi}\begin{pmatrix}P_{qq}&P_{qG}\\ P_{Gq}&P_{GG}\end{pmatrix}\otimes\begin{pmatrix}\Sigma(x,Q^2)\\ xG(x,Q^2)\end{pmatrix}. \tag{86}$$

The splitting functions $P_{ij}(x)$ describe the probability to find a parton i radiated from a parton j and carrying its the momentum fraction x. The diagrams, describing this generically, are depicted in figure 38. The splitting functions are:

$$\begin{aligned}P_{qq}(x) &= C_F\left[\frac{1+x^2}{(1-x)_+}+\frac{3}{2}\delta(1-x)\right]\\ P_{Gq}(x) &= C_F\frac{1+(1-x)^2}{x}\\ P_{qG}(x) &= 2N_fT_R\left[x^2+(1-x)^2\right]\\ P_{GG}(x) &= 2C_G\left[x(1-x)+\frac{1-x}{x}+\frac{x}{(1-x)_+}\right]+\frac{1}{2}\beta_0\delta(1-x).\end{aligned} \tag{87}$$

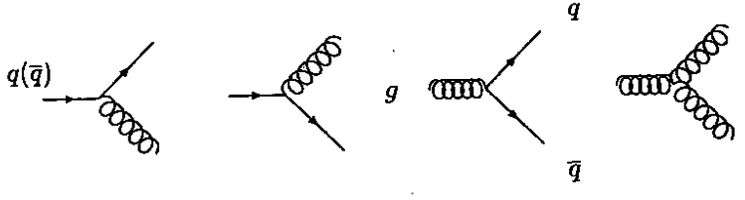

Figure 38: $O(\alpha_s)$ bremsstrahlung diagrams defining the splitting function $P_{ij}(x)$ eq. (87).

Again evolution operators, describing the mapping $f_i(x,Q_0^2\to Q^2)$ can be introduced, which obey

$$\frac{\partial}{\partial\ln Q^2}\begin{pmatrix}E_{FF}&E_{FG}\\ E_{GF}&E_{GG}\end{pmatrix}=\frac{\alpha_s(Q^2)}{2\pi}\begin{pmatrix}P_{qq}&P_{qG}\\ P_{Gq}&P_{GG}\end{pmatrix}\otimes\begin{pmatrix}E_{FF}&E_{FG}\\ E_{GF}&E_{GG}\end{pmatrix} \tag{88}$$

with the initial condition

$$\begin{pmatrix}E_{FF}&E_{FG}\\ E_{GF}&E_{GG}\end{pmatrix}(x,Q^2=Q_0^2)=\delta(1-x)\begin{pmatrix}1&0\\ 0&1\end{pmatrix}. \tag{89}$$

From (87) it becomes clear that for $x \ll 1$ the gluon density will dominate the scaling violations of the structure functions since in leading order the splitting functions $P_{Gi}(x) \sim 1/x$ for $x \to 0$ contrary to the splitting functions $P_{qi}(x)$. In figure 39 this behaviour is illustrated showing the gluonic, valence and sea contribution to $\partial F_2^{em}/\partial \ln Q^2$ separately.

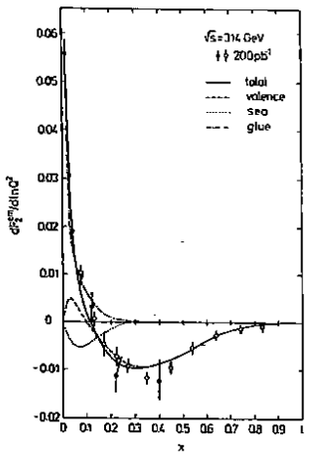

Figure 39: Contributions to the scaling violation of $F_2(x,Q^2)$ due to the valence, sea, and gluon-contribution for a measurement at HERA, [79].

Because of a partial cancellation of the valence and sea terms the gluon contribution dominates by far even at x values as large as 0.1.

In next-to-leading order (NTLO) one may derive similar evolution equations. The splitting functions [80] then become also functions of $\alpha_s(Q^2)$ given by

$$\alpha_s^{NTLO}(Q^2) = \alpha_s^{LO}(Q^2)\left(1 - \frac{\beta_1}{\beta_0^2}\frac{\ln\ln(Q^2/\Lambda^2)}{\ln(Q^2/\Lambda^2)}\right) \tag{90}$$

with $\beta_1 = (34/3)C_G^2 - [(20/3)C_G + 4C_F]T_R N_f$ [81] and

$$P_{ij}\left(x, \frac{\alpha_s(Q^2)}{2\pi}\right) = P_{ij}^{(0)}(x) + \frac{\alpha_s(Q^2)}{2\pi}P_{ij}^{(1)}(x) + \ldots \tag{91}$$

The evolution equations are

$$\frac{\partial f^a(x,Q^2)}{\partial \ln Q^2} = \sum_b P^{ab}\left(x, \frac{\alpha_s(Q^2)}{2\pi}\right) \otimes f_b(x,Q^2) \tag{92}$$

with $f^a(x,Q^2)$ denoting the parton densities.

In the range $x \ll 1$ the splitting functions (91) take the form [82]

$$\begin{aligned} P_{qq}^{(1)}(x) &\propto \frac{1}{x} 2N_f T_R C_F \frac{20}{9} \\ P_{Gq}^{(1)}(x) &\propto \frac{1}{x} 2N_f T_R \left(-\frac{20}{9}\right) + C_F C_G \frac{1}{x} \end{aligned}$$

$$\begin{aligned} P_{qG}^{(1)}(x) &\propto \frac{1}{x} 2N_f T_R C_G \frac{20}{9} \\ P_{GG}^{(1)}(x) &\propto \frac{1}{x} 2N_f T_R \left(-\frac{23}{9} + \frac{2}{3}C_F\right) \end{aligned} \tag{93}$$

Comparing (93) with (87) one notices that also the splitting function describing the evolution of the quark densities behave $\sim 1/x$. Because the sign of the quark splitting functions at small x is positive and that of the gluon splitting functions is negative, the NTLO contributions lower the values of the gluon distribution found in leading order and increase the quark densities. This behaviour is illustrated in figure 40.

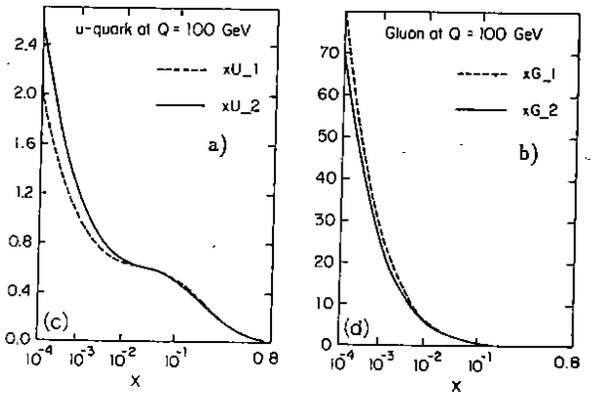

Figure 40: Comparison of first and second order evolved parton distributions. (a) $xu(x,Q)$, (b) $xG(x,Q)$. The input distribution at $Q = 4$ GeV was taken from [35] set 1; [82].

8.1 $e^{\pm}p$ Scattering

Among the possible combinations of quark densities which may be derived from the deep inelastic $e^{\pm}p$ cross sections only a few are suited for a QCD analysis as was shown in [79]. One combination is[15]

$$\begin{aligned} B_+(x,Q^2) &= C_\Sigma(Q^2)\Sigma(x,Q^2) + C_\Delta(Q^2)\Delta(x,Q^2) \\ &= C_\Sigma(Q^2)\left[E_{FF}(x,Q^2)\otimes\Sigma(x,Q_0^2) + E_{FG}(x,Q^2)\otimes G(x,Q_0^2)\right] \\ &+ C_\Delta(Q^2)E_{NS}(x,Q^2)\otimes\Delta(x,Q_0^2) \end{aligned} \tag{94}$$

with

$$\Delta(x,Q^2) = \sum_{i=1}^{N_f/2}\left\{\left[u_i(x,Q^2) + \overline{u}_i(x,Q^2)\right] - \left[d_i(x,Q^2) + \overline{d}_i(x,Q^2)\right]\right\} \tag{95}$$

For $Q^2 \ll M_Z^2$ the functions $C_{\Sigma,\Delta}$ approach $C_\Sigma \to 5/18$ and $C_\Delta \to 1/6$.

In the valence range one finds

$$\begin{aligned} B_+^{val}(x,Q^2) &= C_\Sigma(Q^2)\Sigma(x,Q^2) + E_{FF}(x,Q^2)\otimes\Sigma^{val}(x,Q_0^2) \\ &+ C_\Delta(Q^2)E_{NS}(x,Q^2)\otimes\Delta^{val}(x,Q_0^2) \end{aligned} \tag{96}$$

[15]Below we dropped the arguments Q_0^2 and Λ of the operators E_{ij} for brevity.

which further simplifies to

$$B_+^{val}(x,Q^2) = E_{NS}(x,Q^2) \otimes \left[\frac{5}{18}\Sigma^{val}(x,Q_0^2) + \frac{1}{6}\Delta^{val}(x,Q_0^2)\right] \tag{97}$$

in leading order ($E_{NS} \equiv E_{FF}$) and for $Q^2/M_Z^2 \to 0$. For other combinations of parton densities more complicated evolution equations are obtained in general, i.e. more than one non-singlet initial distribution may be needed. As shown in figure 41 even for an integrated luminosity of $\mathcal{L} = 400pb^{-1}$, e.g., the sum of the up quarks and antiquarks $xU(x,Q^2)$ (and similar examples as well cf. [39]) can not be measured at a statistical precision allowing a QCD analysis.

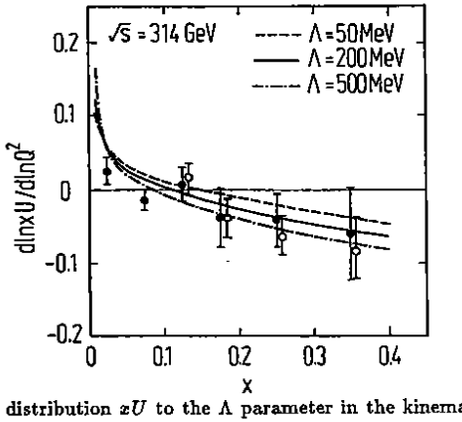

Figure 41: Sensitivity of the distribution xU to the Λ parameter in the kinematical range of HERA (full circles), and non restricted phase space (open circles), [79].

In [34] estimates were derived for the measurement of Λ and α_s in the kinematical range of HERA. To exploit the possibilities given completely, also data at lower s, e.g. $\sqrt{s} = 110\,\mathrm{GeV}$, are required aside those taken at $\sqrt{s} = 314\,\mathrm{GeV}$. We assume $\mathcal{L} = 100pb^{-1}$ for each data sample. The data at low s range to higher values of x at sufficient statistics, allowing a QCD analysis in the valence range. This is well illustrated by the slope $\partial \ln F_2/\partial \ln Q^2$ in figure 42.

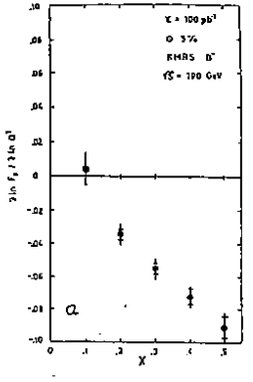

Figure 42: Average slope $\langle \partial F_2/\partial \ln Q^2 \rangle$ vs x in the valence range at HERA. The inner error bars refer to the statistical precision for $\mathcal{L} = 100pb^{-1}$. A 5% systematical error is superimposed, [34].

For the combined data sample $\delta\Lambda \simeq 40\,\mathrm{MeV}$ may be obtained in the kinematical range of HERA taking the cuts $Q^2 \geq 10\,\mathrm{GeV}^2$ and $x \geq 2 \cdot 10^{-3}$ to guarantee deep inelastic scattering and to keep shadowing contributions due to higher twist terms at small x negligibly small. The dependence of $\delta\Lambda$ against x_{min} and Q^2_{min} is illustrated in figure 43.

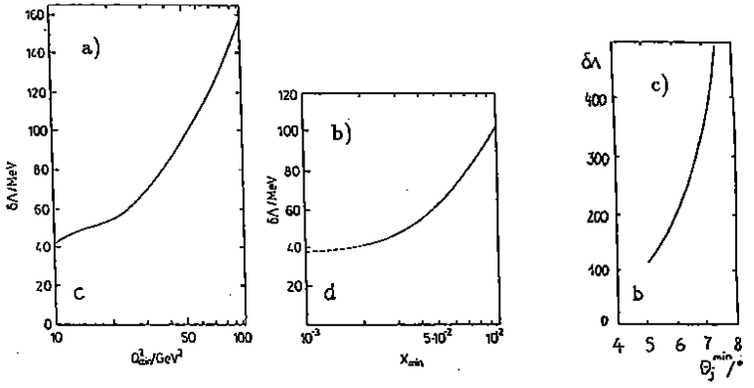

Figure 43: Dependence of $\delta\Lambda_{stat}$ on the minimum Q^2 (a) and x (b) used in the QCD fit for the combined data sets at $\sqrt{s} = 110$ and 314 GeV for $\mathcal{L} = 100pb^{-1}$ each; (c) dependence of $\delta\Lambda_{stat}$ for $x \geq 0.25$, $\mathcal{L} = 100pb^{-1}$, $\sqrt{s} = 110$ GeV on the minimum jet angle; [34].

In the valence range $x \geq 0.25$ one may obtain $\delta\Lambda \simeq 110\,\mathrm{MeV}$ with this combination, if the measurement can be extended down to 5° hadronic jet angle. Because $\delta\Lambda$ is strongly rising with θ_j^{min} (see figure 43 c) a meaningful QCD analysis in the valence range is only possible iff the data are well understood down to $\theta_j^{min} = 5°$.

A similar analysis can be performed at LEP ⊗ LHC. The corresponding results are summarized in terms of α_s values for the different kinematical regions in section 8.3 and compared with the accessible values at HERA and the high energy neutrino experiment.

As shown in [79] miscalibrations of hadronic and/or electromagnetic calorimeters cause systematic errors in Λ as large as the expected statistical errors even if these miscalibrations $\varepsilon_{e,J}$ are globally of the order of a few per cent only. For small y sizeable effects occur in the case of the electron measurement, while for large y the hadron measurement is detoriated. The effect may be of similar size as the QED radiative corrections in some ranges. Because in some part of the kinematical range a simultaneous electron and hadron measurement is possible, one may crosscalibrate respective parts of the calorimeters demanding agreeing cross sections. This has been studied in [83]. The resulting systematic shifts of Λ are much smaller than the statistical error if the cross calibration is carried out.

8.2 νN Scattering

The QCD analysis in a neutrino experiment measuring $xW_3^{\nu N}$, $W_2^{\nu N}(x,Q^2)$, and $\overline{Q}(x,Q^2)$ may be based on the following evolution equations.

$$xW_3(x,Q^2) = E_{NS}(x,Q^2) \otimes V(x,Q_0^2) \tag{98}$$

and

$$
\begin{aligned}
W_2(x,Q^2) &= E_{FF}(x,Q^2) \otimes \left[V(x,Q_0^2) + S(x,Q_0^2)\right] + E_{FG}(x,Q^2) \otimes xG(x,Q_0^2) \\
\overline{Q}(x,Q^2) &= \left[E_{FF}(x,Q^2) - E_{NS}(x,Q^2)\right] \otimes V(x,Q_0^2) \\
&+ E_{FF}(x,Q^2) \otimes S(x,Q_0^2) + E_{FG}(x,Q^2) \otimes xG(x,Q_0^2) \qquad (99)
\end{aligned}
$$

with $\overline{Q}(x,Q^2) = W_2(x,Q^2) - xW_3(x,Q^2) = 2\sum_f x\overline{q}_f(x,Q^2)$ assuming $q_{s_i} \equiv \overline{q}_{s_i}$. Here, the input distributions are $V(x,Q_0^2) = xW_3(x,Q_0^2)$, $S(x,Q_0^2) = W_2(x,Q_0^2) - xW_3(x,Q_0^2)$, and $xG(x,Q_0^2)$ denotes the gluon distribution. Eq. (98) does not contain the gluon distribution and allows to fit Λ together with the parameters of $V(x,Q_0^2)$ in a non–singlet analysis. This information can be used analyzing (99) to determine the shape of the gluon density $xG(x,Q_0^2)$. Performing this analysis under the conditions discussed in section 3 one obtains an accuracy for Λ $\delta\Lambda = 60\,\mathrm{MeV}$ in a non–singlet fit of $xW_3(x,Q^2)$ (98).

8.3 $\alpha_s(Q^2)$

The results of the different QCD analyses can be compared calculating the measured values of α_s. For this purpose the average value of Q^2 has to be determined for the respective data samples. Since the kinematical ranges at HERA, the considered neutrino experiment, and at LEP $\otimes$ LHC are only partly overlapping (see figures 4–6) a similar value of $\langle Q^2 \rangle$ at the three facilities corresponds to a different range in x. Thus, measurements at comparable values of Q^2 but different $\sqrt{s}$ provide a crucial test of the global validity of QCD. In figure 44 a comparison is given for possible α_s measurements in the different kinematical regions at HERA, the neutrino experiment, and LEP $\otimes$ LHC. The data points correspond to an assumed central value of $\Lambda_{\overline{MS}}^{(N_f=4)} = 200\,\mathrm{MeV}$.

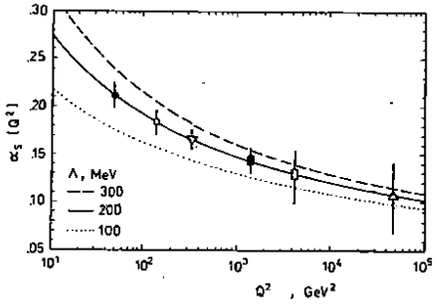

Figure 44: Statistical precision of different possible measurements of $\alpha_s(Q^2)$ in future deep inelastic scattering experiments. The different data points illustrate the sensitivity of: (a) HERA for a combined fit using two data samples $\sqrt{s} = 314\,\mathrm{GeV}$ and $\sqrt{s} = 110\,\mathrm{GeV}$ with $\mathcal{L} = 100pb^{-1}$ each, $\bullet$: $2 \cdot 10^{-3} < x < 0.25$; $\blacksquare$: $x \geq 0.25$, [34]; (b) the neutrino experiment (NS–analysis of $xW_3(x,Q^2)$) (o), [7]; (c) LEP $\otimes$ LHC: $\sqrt{s} = 1.3\,\mathrm{TeV}$ and $\mathcal{L} = 1fb^{-1}$; ∇ : $10^{-4} < x < 10^{-2}$, $\square$: $10^{-2} < x$, and $\triangle$: $x \geq 0.25$, [36]. The drawn lines for $\alpha_s(Q^2)$ correspond to (90) using $\Lambda_{\overline{MS}}^{(N_f=4)}$.

For an integrated luminosity of $\mathcal{L} = 100pb^{-1}$ for both the low energy and design option at HERA the two values of α_s ($\bullet$, $\blacksquare$) determined in the two different kinematical regions are statistically distinct at the level two standard deviations. At LEP $\otimes$ LHC α_s can be measured in the range of both at small x and high Q^2 ranging to several $10^4 \ldots 10^5$ GeV^2. Due to the logarithmic

dependence on Q^2 the precision of the measurements at large Q^2 is small ($\square$,$\triangle$). Otherwise, the statistical precision for the measurement in the range of smaller x (∇) is large. The corresponding data are situated at higher Q^2 values in comparison with the HERA measurement. The neutrino experiment (o) adds a value between the two measurements at HERA with a small statistical error. The three deep inelastic scattering experiments discussed cover three orders of magnitude in Q^2. In the range up to a few 1000 GeV^2 measurements of α_s corresponding to values of $\delta\Lambda = \mathcal{O}(\pm 100\,\mathrm{MeV})$ are possible.

8.4 Constraints on the Gluon Density

The shape of the gluon distribution at Q_0^2 is determined in QCD analyses (see eqs. (94,99)) as a fourth method [16]. The gluon distribution at Q_0^2 may be *basically* characterized by three parameters [17]: the normalization A_G, and the powers α and β determining its basic behaviour for $x \to 0$ and $x \to 1$.

$$xG(x,Q_0^2) = A_G x^{\alpha}(1-x)^{\beta} \qquad (100)$$

A_G is related to α and β by the momentum sum rule $\int_0^1 xG(x,Q_0^2)dx \simeq 1/2$. In QCD analyses of data sets from high energy experiments (HERA and LEP $\otimes$ LHC) the sensitivity to β turns out to be rather weak. On the other hand, Λ and α are strongly correlated and have to be determined simultaneously.

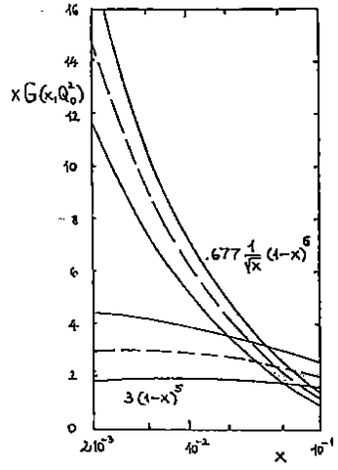

Figure 45: Possible determination of $xG(x,Q_0^2)$ in a QCD fit of $F_2(x,Q^2)$ in the kinematical range of HERA for $2 \cdot 10^{-3} < x < 0.1$. The upper error band corresponds to the statistical error for the choice $\alpha = -0.5$ and the lower band to $\alpha = 0$ for $\mathcal{L} = 100pb^{-1}$ both for the high and low energy option; [34].

Particularly, it will be possible under the conditions lined out in section 3 to distinguish between

[16] A further method to derive information on $xG(x,Q^2)$ consists in using its relation to $\partial F_2/\partial \ln Q^2$. As shown in figure 39 ([79]) the contribution by $xG(x,Q^2)$ to $\partial F_2/\partial \ln Q^2$ is dominating for $x \leq 0.1$ in the kinematical range at HERA. This method has been proposed first by Baulieu and Kounnas [84] and was applied to data in [42] already some time ago. Recently, a simplified relation has been given in [85], similar to the approach [56] for F_L in lowest order QCD.

[17] In a global data analysis more parameters are required in general to fix $xG(x,Q_0^2)$ in all details [50]–[52].

a flat $\alpha \simeq 0$ or a rising $\alpha \simeq -0.3... - 0.5$ input distribution $xG(x,Q_0^2)$ via a QCD analysis [86, 36, 34]. In figure 45 the statistical precision for the determination of $xG(x,Q_0^2)$ is depicted for a measurement at HERA. The combined analysis of the data set at $\sqrt{s} = 110\,\mathrm{GeV}$ and $\sqrt{s} = 314\,\mathrm{GeV}$ demanding $2\cdot10^{-3} < x < 0.1$ yields $\delta\alpha = \pm 0.1$. Similar results for $xG(x,Q_0^2)$ were derived under for the conditions at LEP $\otimes$ LHC [36] and the high energy neutrino experiment [7]. In the small x range narrow constraints for $xG(x,Q_0^2)$ can be obtained at LEP $\otimes$ LHC. The estimated bounds in the neutrino experiment are weaker at smaller x, but cover the range of larger x values.

8.5 Results on α_s from other Experiments

The strong coupling constant $\alpha_s(Q^2)$ has been measured in the past using a variety of different methods. Besides deep inelastic $\nu(\overline{\nu})N$ and $l^{\pm}$ scattering, the branching ratio $R_\tau = B(\tau \rightarrow hadrons + \nu_\tau)\,/B(\tau \rightarrow e\,\overline{\nu}_e\,\nu_\tau)$, J/ψ and Υ decays into gluons, the hadronic annihilation cross section, event shape measurements, and scaling violations in e^+e^- scattering, the beauty and $W + jet$ cross sections $p\overline{p} \rightarrow b\overline{b}X$ and $p\overline{p} \rightarrow W + jets$, the hadronic decay width of the Z–boson, and Z–event shapes have been used to determine α_s. The renormalization group equation allows to rescale the different measurements choosing a single scale, e.g. $\hat{Q}^2 = M_Z^2$, for a comparison. A recent compilation of the different α_s measurements has been provided by S. Bethke [87]. In Figure 46 the values of $\alpha_s(M_Z^2)$ are summarized [87].

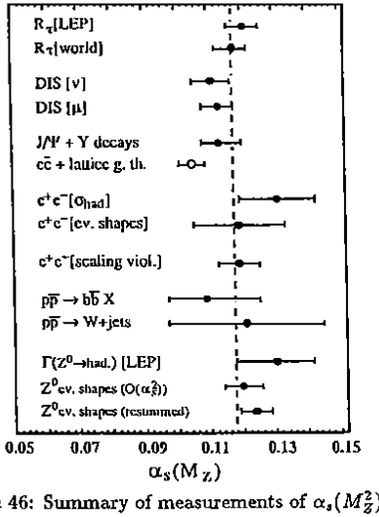

Figure 46: Summary of measurements of $\alpha_s(M_Z^2)$, [87].

As lined out in [87] these data can all be described with Λ values in the range $150 < \Lambda^{(5)}_{\overline{MS}} < 250\,\mathrm{MeV}$ corresponding to $\delta\alpha_s(M_Z) = \pm 0.004$. Taking a more pessimistic point of view the required range for Λ would be $100 < \Lambda^{(5)}_{\overline{MS}} < 350\,\mathrm{MeV}$ yielding $\delta\alpha_s = \pm 0.011$.

Since the contribution of theoretical uncertainties to $\alpha_s(M_Z)$ are rather large it is difficult to 'derive' the error of the world average of the different α_s measurements. Averaging the above α_s errors one obtains [87]

$$\alpha_s(M_Z^2) = 0.118 \pm 0.007 \tag{101}$$

A similar result was given by G. Altarelli [88]

$$\alpha_s(M_Z^2) = 0.117 \pm 0.007 \tag{102}$$

Here, the error is an estimate of the typical theoretical uncertainty.

9 The Onset of Shadowing at Small x

In the small–x range the GLAP–evolution equations yield solutions which eventually violate unitarity. This can be seen most easily solving (86) for $x \rightarrow 0$ for only the gluon density. The contributions due to the quark densities can be neglected because they are of subleading order (see figure 39). The splitting function $P_{GG}(x)$ is approximated by its most singular part $P_{GG}(x) \propto P_{GG}^{x\rightarrow 0}(x) = 2C_G/x$ leading to

$$\frac{\partial}{\partial \log Q^2} xG(x,Q^2) = \frac{\alpha_s(Q^2)}{2\pi}\frac{2C_G}{x} \otimes xG(x,Q^2) \tag{103}$$

Differentiating (103) for $\ln(x)$ one obtains the hyperbolic partial differential equation [89]

$$\frac{\partial^2}{\partial\xi\partial y}\mathcal{G}(y,\xi) = \frac{1}{2}\mathcal{G}(y,\xi) \tag{104}$$

with $\mathcal{G}(y,\xi) \equiv xG(x,Q^2)$ in the variables:

$$y = \frac{8C_G}{\beta_0}\log\left(\frac{1}{x}\right) \qquad\qquad \xi = \ln\ln\left(\frac{Q^2}{\Lambda^2}\right) \tag{105}$$

The general solution of (104) is [90]

$$\mathcal{G}(y,\xi) = \sum_{\nu=0}^{\infty}\left\{A_\nu\left(\frac{2\xi}{y}\right)^{\nu/2} + B_\nu\left(\frac{y}{2\xi}\right)^{\nu/2}\right\} I_\nu\left(\sqrt{2y\xi}\right) \tag{106}$$

The constants A_ν and B_ν have to be determined from the non–perturbative initial condition at $\xi_0 = \xi(Q_0^2)$. Because the modified Bessel functions $I_\nu(z)$ behave like $I_\nu(z) \sim \exp(z)/\sqrt{2\pi z}\,[1 - (4\nu^2-1)/(8z) + \mathcal{O}(z^{-2})]$ for $x \rightarrow 0$, $\mathcal{G}(y,\xi)$ grows faster than any power of $y \propto \ln(1/x)$.

This behaviour is modified taking into account the NTLO term $\propto 1/x$ for $P_{GG}(x,\alpha_s)$ (93) also which introduces the factor

$$P_{GG}^{x\rightarrow 0}(x,\alpha_s) = P_{0,GG}^{x\rightarrow 0}(x) \times \left[1 - \frac{\alpha_s(Q^2)}{2\pi}\frac{N_f T_R}{C_G}\left(\frac{23}{9} - \frac{2}{3}C_F\right)\right] \tag{107}$$

in (103) leading to a smaller groth of $\mathcal{G}(y,\xi)$ (cf. figure 40). However, the above argument remains unchanged.

If the parton (gluon) densities at smaller and smaller x become very large also the probability of parton recombination grows. This leads to a reduction of the parton densities.

An equation describing this behaviour has been suggested a decade ago by Gribov, Levin, and Ryskin [91]. This equation

$$\frac{\partial^2}{\partial\xi\partial y}\mathcal{G}(y,\xi) = \frac{1}{2}\mathcal{G}(y,\xi) - C\exp\left[-(e^\xi + \xi)\right]\mathcal{G}^2(y,\xi), \tag{108}$$

with $\mathcal{C} = [(3\pi^2)/(4\beta_0)](Q_0^2/\Lambda^2)$ [92], has been investigated numerically in [93, 94]. The exponential in (108) may be rewritten as

$$\exp\left[-(e^\xi + \xi)\right] = \frac{1}{\ln(Q^2/\Lambda^2)}\frac{\Lambda^2}{Q^2}. \tag{109}$$

Thus, the solution of eq. (108) contains a summation over higher twist ($\propto (1/Q^2)^n$) terms to arbitrary order.

Eq. (108) may be cast into the integral form

$$\mathcal{G}(y,\xi) = \mathcal{G}(y,\xi_0) + \int_{\xi_0}^{\xi} d\xi' \int_0^y y' \mathcal{G}(y',\xi') \left\{\frac{1}{2} - \mathcal{C}\exp\left[-(e^\xi + \xi)\right] \mathcal{G}(y,\xi)\right\}. \tag{110}$$

The solution of (110) posesses the following general properties: *(i)* it is bounded from above by the corresponding solution of eq. (104) ($\mathcal{C} = 0$) if the same initial condition is used; *(ii)* the solution is unique (see [93]); *(iii)* in the limit $x \to 0$ $\mathcal{G}(y,\xi)$ approaches a value which is independent of the choosen input distribution $\mathcal{G}(y,\xi_0)$:[18]

$$\lim_{y\to\infty} \mathcal{G}(y,\xi) = \frac{1}{2\mathcal{C}}\exp\left[e^\xi + \xi\right] = \frac{2\beta_0}{3\pi^2}\frac{Q^2}{Q_0^2}\log\left(\frac{Q^2}{\Lambda^2}\right), \tag{111}$$

i.e. $\mathcal{G}(y,\xi)$ saturates for $x \to 0$.

The effect of shadowing can be searched for in different inclusive and semi-inclusive [95] measurements in the small x range. Here we will concentrate on the case of the measurement of $F_2(x,Q^2)$.

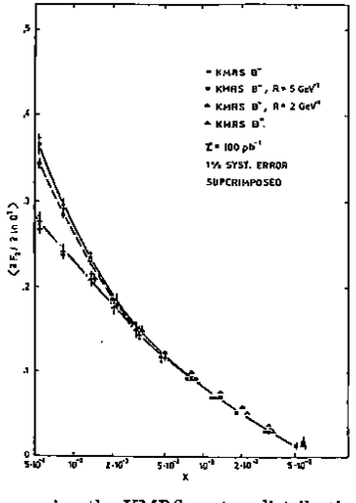

Figure 47: Average slope of F_2 vs x using the KMRS parton distributions. Full line: B^- no screening; dashed line: B^- weak ($R = 5\,\mathrm{GeV}^{-1}$) screening; dash dotted line: B^- strong ($R = 2\,\mathrm{GeV}^{-1}$). The statistical error (inner error bars) corresponds to $\mathcal{L} = 100pb^{-1}$ and a systematical error of 1 % is superimposed; [34].

[18]Note, however, that the physical range of validity, for which (108) originally had been derived, is bounded by $2\mathcal{C}\exp\left[-(e^\xi + \xi)\right] \lesssim 1$.

As shown in section 5.1 this structure function can be measured with high precision at small x. Thus, the slope $\langle \partial F_2(x,Q^2)/\partial \ln Q^2\rangle$ can serve as a possible observable to investigate shadowing effects. This is illustrated in figure 47 where predictions are compared assuming different screening radii $R = 1/Q_0$ in the KMRS–parametrization [32] taking into account (108). From these parametrizations screening effects are expected to be very small in the range $x \gtrsim 2\cdot 10^{-3}$. Therefore, one can determine the shape of the gluon distribution at Q_0^2 in this range (see section 8). The parton densities $f_a(x,Q_0^2)$ determined in the range $x > x_{min} \approx 2\cdot 10^{-3}$ can be used as an input for the GLAP–evolution equations to calculate the expectation for $\langle \partial F_2(x,Q^2)/\partial \ln Q^2\rangle_{GLAP}$ in the range of $x < x_{min}$. If the measured values of $\langle \partial F_2(x,Q^2)/\partial \ln Q^2\rangle$ turn out to be smaller than the extrapolation this would be a signal for shadowing. As shown in figure 47 the shadowing effect should be clearly visible for $R = 2\,\mathrm{GeV}^{-1}$, while for $R = 5\,\mathrm{GeV}^{-1}$ the measurement will be more difficult.

The estimate given in figure 47 is still preliminary, and further detailed quantitative studies are required. This is due to the following reasons. In recent investigations it was shown [96] that the description of shadowing (108,110) has to be supplemented by further terms. In general it may even turn out that the shadowing of the gluon distribution can not be described by a single (nonlinear) equation. Furthermore, most of the recent efforts were concentrating on the derivation of evolution kernels in the small–x approximation. However, since the evolution operators and parton distributions are connected by a convolution ($\otimes$) in x space (82,86,92) the kernels have to be known also in the range of larger x values [61] and small and 'large' x effects have to be encountered in the evolution equations simultaneously [97].

10 First Results from HERA

The HERA experiments H1 and ZEUS are the first experiments which have detected deep inelastic events in the range of very small $x \sim 10^{-4}$. Currently ~ 1000 deep inelastic events have been analyzed by each of the experiments [98, 99][19]. The statistics is situated dominantly in the range $x \lesssim 10^{-2}$ and $Q^2 \lesssim 100\,\mathrm{GeV}^2$. So far only single events in the range of high Q^2 have been detected, among them a charged current candidate with $Q^2 \sim 14.000\,\mathrm{GeV}^2$ by ZEUS.

The structure function $F_2(x,Q^2)$ has been measured from these data under some assumptions on $R(x,Q^2) = F_L(x,Q^2)/2xF_1(x,Q^2)$. The kinematical variables x and Q^2 have been measured by different methods. In the H1 experiment they were determined either by the measurement of the scattered electron or measuring Q^2 from the scattered electron and y from the current jet. The ZEUS experiment used the double angle method, i.e. $\theta_{e'}$ and θ_{Jet} to reconstruct the event kinematics. As discussed in section 4 already the QED radiative corrections to all these three methods are completely different. The measured values for $F_2(x,Q^2)$ determined by these different methods are found to agree within the experimental errors.

In figure 48 the result of this measurement is shown. At constant Q^2 $F_2(x,Q^2)$ rises rapidly towards small x. Otherwise the observed scaling violations behave logarithmic as described by the GLAP–equations within the current experimental errors. The current statistics is still rather limited. To obtain a sufficient number of events in the overlap region with the kinematical range probed by the fixed target experiments more statistics is required. However, during the next year a rise in the statistics by about a factor of 50 is expected. These data will allow to give a rather detailed picture on the behaviour of the nucleon structure in the small x range already.

[19]Results on the deep inelastic scattering cross sections based on a statistics of the first $\sim$ 100 events were published in [100].

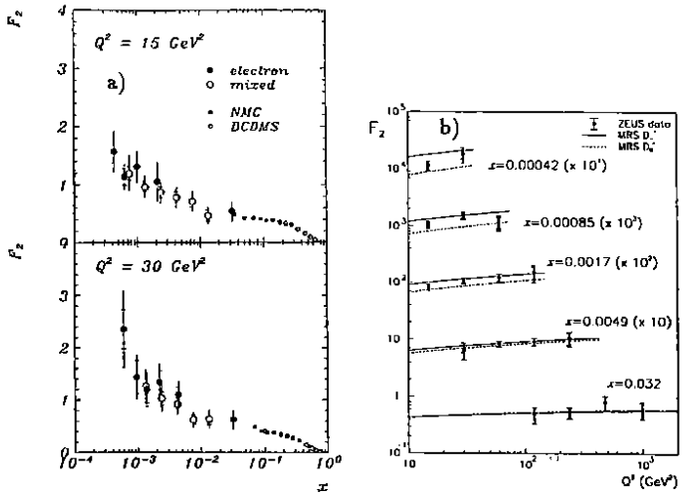

Figure 48: (a) Measurement of $F_2(x, Q^2)$ for two values of Q^2 by the H1 experiment. The full circles correspond to the electron measurement, and the open circles to the method of mixed variable. The inner error bars denote the statistical errors, the outer bar shows the systematic error added in quadrature. An overall normalization uncertainty of 8 % is not included. Data points of the fixed target μp scattering experiments NMC [101] and BCDMS [102] are shown for comparison, from [98];
(b) The structure function $F_2(x, Q^2)$ as a function of Q^2 for different values of x measured by ZEUS. The inner error bars denote the statistical errors, the outer bar shows the systematic error added in quadrature. An overall normalization uncertainty of 7 % is not included, from [99].

11 Conclusions

With the start of the HERA experiments a novel era in the investigation of the proton structure has begun. Compared to the fixed target νN and $l^{\pm}N$ experiments performed during the last two decades the accessible kinematical range will be extended by about two orders of magnitude both in x and Q^2. At LEP $\otimes$ LHC one can extend this range even further by another order of magnitude. In this way both the investigation of the nucleon structure at very small distances $\sim 1/Q$ and huge energies $\sim 1/x$ is possible.

The major topics to be investigated are: the test of the validity of Quantum Chromodynamics at *(i)* high Q^2, at *(ii)* small x, and *(iii)* the detailed measurement of the flavour and gluon substructure of the nucleons.

In the small x range new dynamical effects modifying the GLAP evolution can be searched for. Different methods exist to extract the gluon distribution. Aside of the study of the scaling violations of structure functions it can be derived from measurements of the longitudinal structure function $F_L(x, Q^2)$ and the heavy flavour and J/ψ production cross sections down to the range of very small x. The detailed knowledge of this quantity is very important for many investigations to be performed at the future proton–colliders SSC and LHC. The flavour structure of the quark sector can be precisely investigated in charged current scattering. Future high energy neutrino experiments can supplement the studies performed with $e^{\pm}N$ colliders to obtain

detailed measurements in a wide kinematical range.

The present and possible future facilities to study the structure of nucleons via deep inelastic scattering offer partly complementary possibilities. At HERA the small x structure of the nucleon is probed for the first time. At LEP $\otimes$ LHC this range may be probed at even smaller x values. Furthermore, in the range of high Q^2 a large statistics is expected compared with the possibilities at HERA which allows to measure different combinations of quark distributions at very high Q^2. Otherwise, the lower range of $Q^2 \sim \mathcal{O}(0.5...1\,\mathrm{TeV})$ can be covered by new high energy neutrino experiments.

In this way our understanding of the structure of matter can be completed furtheron. Aside of the scientific aspect this search serves a philosophical purpose as expressed in Dr. Faustus' monologue:

Daß ich erkenne was die Welt
Im Innersten zusammenhält,
Schau' alle Wirkenskraft und Samen
Und thu' nicht mehr in Worten kramen.

Acknowledgement
Many of the results presented in this lecture have been derived in collaboration with colleagues during the recent years. For various discussions and conversations I would like to thank D.Y. Bardin, J. Bartels, E. Reya, G. Ingelman, M. Klein, E.M. Levin, L.N. Lipatov, A.H. Mueller, W.L. van Neerven, T. Riemann, R. Rückl, G. Schuler, and Wu–Ki Tung. My thanks are due to D.I. Diakonov and Y.I. Azimov for the skilled organization of the Winter School and all the St. Petersburg colleagues for the warm hospitality extended to me.

References

[1] E.D. Bloom et al., Phys. Rev. Lett. **23** (1969) 930;
M. Breidenbach et al., Phys. Rev. Lett. **23** (1969) 935;
R.E. Taylor, Rev. Mod. Phys. **63**, 573 (1991);
H.W. Kendall, Rev. Mod. Phys. **63**, 597 (1991);
J.I. Friedman, Rev. Mod. Phys. **63**, 615 (1991).

[2] For reviews see:
F. Eisele, Rep. Progr. Phys. **49**, 233 (1986);
M. Diemoz, F. Ferroni, and E. Longo, Phys. Rep. **130**, 293 (1986);
T. Sloan, G. Smadja, and R. Voss, Phys. Rep. **162**, 45 (1988).

[3] R.P. Feynman, Phys. Rev. Lett. **23** (1969) 1415;
S.D. Drell and Tung–Mow Yan, Phys. Rev. Lett. **22** (1969) 744; Phys. Rev. **187** (1969) 2159; Phys. Rev. **D1** (1970) 1035; 1617; 2402; Ann. Phys. (New York) **66** (1971) 578.

[4] see e.g.: E. Derman, Phys. Rev. **D7** (1973) 2755.

[5] J.D. Bjorken, Phys. Rev. **179** (1969) 1547.

[6] C.G. Callen and D.J. Gross, Phys. Rev. Lett. **22** (1969) 156.

[7] J. Blümlein, M. Walter, M.M. Kirsanov, and A.S. Vovenko, Acta Physica Hungarica **68** (1990) 95.

[8] J. Blümlein, J. Feltesse, and M. Klein, Proceedings of the 'ECFA Large Hadron Collider Workshop', Aachen 4–9 October 1990, eds. G. Jarlskog and D. Rein, CERN 90–10, ECFA 90–133, Vol. **2**, (CERN, Geneva, 1991), p. 830.

[9] M. Klein, in: Proc. of the 1992 HERA Workshop, Vol. **1**, eds. W. Buchmüller and G. Ingelman, (DESY, Hamburg, 1992), p. 71.

[10] G. Schuler, F. Olness, J. Blümlein, and Wu–Ki Tung, Proceedings 'Research Directions of the Decade', Snowmass,CO, June 25–July 14 1990, ed. E.L Berger, (World Scientific, Singapore, 1992), p. 152.

[11] J. Blümlein, M. Klein, Th. Naumann, and T. Riemann, Proc. of the HERA Workshop, Hamburg, October 1987, ed. R.D. Peccei, Vol. **1**, p. 67.

[12] G. Ingelman, Proceedings of the 'ECFA Large Hadron Collider Workshop', Aachen 4–9 October 1990, eds. G. Jarlskog and D. Rein, Vol. **2**, (CERN, Geneva, 1991), CERN 90–10, ECFA 90–133, p. 834.

[13] H. Spiesberger, et al., in: Proc. of the 1992 HERA Workshop, Vol. **2**, eds. W. Buchmüller and G. Ingelman, (DESY, Hamburg, 1992), p. 798.

[14] D. Bardin, O. Fedorenko, and N. Shumeiko, J. Phys. **G7** (1981) 1331;
D. Bardin, C. Burdik, P. Christova, and T. Riemann, Dubna preprint E2–87–595;
D. Bardin, A. Akhundov, L. Kalinovskaya, and T. Riemann, in: Proc. of the Workshop 'Deep Inelastic Scattering', Teupitz, Brandenburg, April 1992, eds. J. Blümlein and T. Riemann, Nucl. Phys. **B** (Proc. Suppl.) **29A** (1992) 209;
D. Bardin, C. Burdik, P. Christova, and T. Riemann, Z. Phys. **C44** (1989) 149.

[15] D. Bardin, C. Burdik, P. Christova, and T. Riemann, Z. Phys. **C42** (1989) 679.

[16] M. Böhm and H. Spiesberger, Nucl. Phys. **B294** (1987) 1081; **B304** (1987) 749;
H. Spiesberger, in: Proc. of the 13th Int. School of Theor. Phys. Szczyrk, Poland, 1989, p. 145;
H. Spiesberger, Nucl. Phys. **B349** (1991) 109;
A. Kwiatkowski, H.–J. Möhring, and H. Spiesberger, in: Proc. of the 1992 HERA Workshop, Vol. **3**, eds. W. Buchmüller and G. Ingelman, (DESY, Hamburg, 1992), p. 1294;
H. Spiesberger, in: Proc. of the Workshop 'Deep Inelastic Scattering', Teupitz, Brandenburg, April 1992, eds. J. Blümlein and T. Riemann, Nucl. Phys. **B** (Proc. Suppl.) **29A** (1992) 221;
H. Anlauf, P. Manakos, T. Mannel, H.D. Dahmen, and T. Ohl, ibid. p. 247.

[17] J. Blümlein, Z. Phys. **C47** (1990) 89;
J. Blümlein, in: Proceedings of the 'ECFA Large Hadron Collider Workshop', Aachen 4–9 October 1990, eds. G. Jarlskog and D. Rein, Vol. **2**, (CERN, Geneva, 1991), CERN 90–10, ECFA 90–133, p. 850.

[18] W. Beenakker, F. Berends, and W. van Neerven, in: 'Radiative Corrections for e^+e^- Colliders', ed. J.H. Kühn, (Springer, Berlin, 1989), p. 3.

[19] E. Kuraev, N. Merenkov, and V. Fadin, Sov. J. Nucl. Phys. **47** (1988) 1009;
G. Montagna, O. Nicrosini, and L. Trentadue, Nucl. Phys. **B357** (1991) 390.

[20] J. Blümlein, Phys. Lett. **B271** (1991) 267.

[21] J. Blümlein, DESY–report, 1993.

[22] J. Kripfganz, H.–J. Möhring, and H. Spiesberger, Z. Phys. **C49** (1991) 501.

[23] J. Blümlein, in: Proc. of the 1992 HERA Workshop, Vol. **3**, eds. W. Buchmüller and G. Ingelman, (DESY, Hamburg, 1992), p. 1269.

[24] T. Kinoshita, J. Math. Phys. **3** (1962) 650;
T.D. Lee and M. Nauenberg, Phys. Rev. **133** (1964) B1549.

[25] A. Akhundov, D. Bardin, L. Kalinovskaya, and T. Riemann, in: Proc. of the 1992 HERA Workshop, Vol. **3**, eds. W. Buchmüller and G. Ingelman, (DESY, Hamburg, 1992), p. 1285.

[26] A. Akhundov, D. Bardin, L. Kalinovskaya, and T. Riemann, Phys. Lett. **B301** (1993) 447.

[27] A. De Rujula, R. Petronzio, and A. Savoy–Navarro, Nucl. Phys. **B154** (1979) 394.

[28] J. Kripfganz and H. Perlt, Z. Phys. **C41** (1988) 319.

[29] J. Blümlein, G. Levman, and H. Spiesberger, in: Proceedings 'Research Directions of the Decade', Snowmass,CO, June 25–July 14 1990, ed. E.L Berger, (World Scientific, Singapore, 1992), p. 554.

[30] J. Blümlein, G. Levman, and H. Spiesberger, J. Phys. **G** (1993), in press.

[31] W.J. Marciano and A. Sirlin, Nucl. Phys. **B189** (1981) 442; Phys. Rev. **D22** (1980) 2695, Erratum: ibid. **D31** (1985) 213; Nucl. Phys. **B217** (1983) 84;
J.F. Wheater and C.H. Llewellyn–Smith, Nucl. Phys. **B208** (1982) 27;
E.A. Paschos and M. Wirbel, Nucl. Phys. **B194** (1982) 189;
M. Wirbel, Z. Phys. **C14** (1982) 293;
I. Liede, E.A. Paschos, M.Roos, and S. Sakakibara, HUTFT–83–45;
D. Bardin and V. Dokuchaeva, Sov. J. Nucl. Phys. **36** (1982) 282; Dubna Preprint JINR E2–86–260;
J. Blümlein and M. Walter, ν–CAL–Note, 89–04/01, IfH–Zeuthen, (1989).

[32] J. Kwiecinski, A. Martin, W. Stirling, and R. Roberts, Phys. Rev. **D42** (1990) 798.

[33] J. Blümlein, talk given at the 1991 HERA Physics Workshop, and [34].

[34] J. Blümlein and M. Klein, in: Proc. of the 1992 HERA Workshop, Vol. **1**, ed. W. Buchmüller and G. Ingelman, (DESY, Hamburg, 1992), p. 101.

[35] E. Eichten, I. Hinchcliffe, K. Lane, and C. Quigg, Rev. Mod. Phys. **56** (1984) 579, Erratum: ibid. **58** (1986) 1065.

[36] J. Blümlein, in: Proceedings of the 'ECFA Large Hadron Collider Workshop', Aachen 4–9 October 1990, eds. G Jarlskog and D. Rein, CERN 90–10, ECFA 90–133, Vol. **2** (CERN, Geneva, 1991), p. 897.

[37] H. Deden et al., BEBC–collaboration, Phys. Lett. **B98** (1981) 310;
P.C. Bosetti et al., BEBC–collaboration, Nucl. Phys. **B217** (1983) 1;
M.D. Jones et al., E546–collaboration, UH–511–531–84;
J.V. Allaby et al., CHARM–collaboration, Z. Phys. **C36** (1987) 611; Phys. Lett. **B213** (1988) 554;
A. Blondel et al., CDHS–collaboration, Z. Phys. **C45** (1990) 361;
M. Aderholz et al., E632–collaboration, Phys. Rev. **D45** (1992) 2232;
K. Winter (ed.), *Neutrino Physics*, §5.9, M. Diemoz, F. Ferroni, E. Longo, and G. Martinelli: Neutral–current structure functions.

[38] F. Olness and Wu–Ki Ting, Nucl. Phys. **B308** (1988) 813.

[39] G. Ingelman and R. Rückl, Phys. Lett. **B201** (1988) 369; Z. Phys. **C44** (1989) 291.

[40] G. Ingelman and R. Rückl, in: Proc. of the HERA Workshop, Hamburg, October 1987, ed. R.D. Peccei, Vol. **1**, p. 107.

[41] E. Witten, Nucl. Phys. **B104** (1976) 445;
M.A. Shifman, A.I. Vainshtein, and V.I. Zakharov, Nucl. Phys. **B136** (1978) 157;
J.P. Leveille and T. Weiler, Nucl. Phys. **B147** (1978) 147;
T. Gottschalk, Phys. Rev. **D23** (1981) 56;
M. Glück, R.M. Godbole, and E. Reya, Z. Phys. **C38** (1988) 441, Erratum ibid. **C39** (1988) 590;
G. Schuler, Nucl. Phys. **B299** (1988) 21;
U. Baur and J.J. van der Bij, Nucl. Phys. **B304** (1988) 451;
R.A. Eichler and Z. Kunszt, Nucl. Phys. **B308** (1988) 791;
For reviews see:
A. Ali et al., in: Proc. of the HERA Workshop, Hamburg, October 1987, ed. R.D. Peccei, Vol. **1**, p. 395;
A. Ali and D. Wyler, in: Proc. of the 1991 HERA Workshop, Vol. **2**, eds. W. Buchmüller and G. Ingelman, (DESY, Hamburg, 1992), p. 669;
A. Ali in: Proc. of the Workshop 'Deep Inelastic Scattering', Teupitz, Brandenburg, April 1992, eds. J. Blümlein and T. Riemann, Nucl. Phys. **B** (Proc. Suppl.) **29A** (1992) 169.

[42] M. Glück, E. Hoffmann, and E. Reya, Z. Phys. **C13** (1982) 119.

[43] J.C. Collins and Wu–Ki Tung, Nucl. Phys. **B278** (1986) 934.

[44] J. Blümlein, G.J. van Oldenborgh, and R. Rückl, Nucl. Phys. **B395** (1993) 35.

[45] see e.g.:
J. Kuti and V.F. Weisskopf, Phys. Rev. **D4** (1971) 3418;
J. Pakvasa, D. Parashar, and S.F. Tuan, Phys. Rev. **D10** (1974) 2124;
R.F. Peierls, T.L. Trueman, and L.L. Wang, Phys. Rev. **D16** (1977) 1397;
R.D. Field and P.R. Feynman, Phys. Rev. **D15** (1977) 2590;
V. Barger, W.Y. Keung, and R.J.N. Phillips, Phys. Rev. **D24** (1981) 244;
D.P. Roy, Phys. Rev. Lett. **47** (1981) 213.

[46] A.J. Buras and K.J.F. Gaemers, Nucl. Phys. **B132** (1978) 249.

[47] J.F. Owens and E. Reya, Phys. Rev. **D17** (1978) 3003;
R. Baier, J. Engels, and B. Petersson, Z. Phys. **C2** (1979) 265;
M. Glück et al ref. [42];
D.W. Duke and J.F. Owens, Phys. Rev. **D30** (1984) 49;
E. Eichten et al., ref. [35];
M. Diemoz, F. Ferroni, E. Longo, and G. Martinelli, Z. Phys. **C39** 21 (1988);
A.D. Martin, R.G. Roberts, and W.J. Stirling, Phys. Rev. **D37** (1988) 1161; Phys. Lett. **B206** (1988) 327; Mod. Phys. Lett. **A4** (1989) 1135;
P. Aurenche, R. Baier, M. Fontannez, J.F. Owens, and M. Werlen, Phys. Rev. **D39** (1989) 3275;
P. Aurenche, R. Baier, M. Fontannez, M.N. Kienzle–Focacci, and M. Werlen, Phys. Lett. **B233** (1989) 517;
P.N. Harriman, A.D. Martin, W.J. Stirling, and R.G. Roberts, Phys. Rev. **D42** 798 (1990), Phys. Lett. **B243** (1990) 421;
M. Glück, E. Reya, and A. Vogt, Z. Phys. **C48** (1990) 471;
J. Kwiecinski et al. ref. [32];
A.D. Martin, R.G. Roberts, and W.J. Stirling, Phys. Rev. **D43** (1991) 3648;
J. Morfin and Wu–Ki Tung, Z. Phys. **C52** 13 (1991);
J.F. Owens, Phys. Lett. **B266** 126 (1991);
P.J. Sutton, A.D. Martin, R.G. Roberts, and W.J. Stirling, Phys. Rev. **D45** (1992) 2349;
A.D. Martin, W.J. Stirling, and R.G. Roberts, Phys. Rev. **D47** (1993) 867.

[48] M. Glück and E. Reya, Phys. Rev. **D14** (1976) 3034; E. Reya, Phys. Rep. **C69** (1981) 195, sect. 5.6.;
G. Parisi and N. Sourlas, Nucl. Phys. **B151** (1979)421;
L.F. Abbott, W.B. Atwood, and R.M. Barnett, Phys. Rev. **D22** (1980) 582;
K. Kato, Y. Shimizu, and H. Yamamoto, Progr. Theor. Phys. **63** (1980) 1295;
K. Kato and Y. Shimizu, Progr. Theor. Phys. **64** (1980) 703;
F.J. Ynduráin, Phys. Lett. **B74** (1978) 68;
A. González–Arroyo, C. López, and F.J. Ynduráin, Nucl. Phys. **B153** (1979) 161; **B159** (1979) 512; **B174** (1980) 474;
A. González–Arroyo and C. López, Nucl. Phys. **B166** (1980) 429;
W. Furmanski and R. Petronzio, Nucl. Phys. **B195** (1982) 237;
A. Devoto, D.W. Duke, J.F. Owens, and R.G. Roberts, Phys. Rev. **D27** (1983) 508;
J. Chyla and J. Rames, Czech. J. Phys. **B36** (1986) 567; Z. Phys. **C31** (1986) 151;
M. Virchaux and A. Oraou, Saclay preprint DPhPE 87–15;
V.G. Krivokhizhin, S.P. Kurlovich, V.V. Sanadze, I.A. Savin, A.V. Sidorov, and N.B. Skachkov, Z. Phys. **C36** (1987) 51;
Wu–Ki Tung et al., CTEQ QCD evolution program, unpublished.

[49] A.C. Benvenuti et al., BCDMS–collaboration, Phys. Lett. **B195** (1987) 97.

[50] M. Glück, E. Reya, and A. Vogt, Z. Phys. **C53** (1992) 127.

[51] J. Botts, J.G. Morfin, J.F. Owens, J. Qiu, Wu–Ki Tung, and H. Weerts, CTEQ collaboration, Phys. Lett. **B304** (1993) 159.

[52] A.D. Martin, W.J. Stirling, and R.G. Roberts, Phys. Lett. **B306** (1993) 145, Erratum: ibid. **B309** (1993) 492.

[53] H. Plothow–Besch, Comp. Phys. Comm. **75** (1993) 396.

[54] A.D. Martin, W.J. Stirling, and R.G. Roberts, Phys. Lett. **B308** (1993) 377.

[55] A. Zee, F. Wilczek, and S.B. Treiman, Phys. Rev. **D10** (1974) 2881.

[56] A. Cooper–Sarkar, G. Ingelman, K.R. Long, R.G. Roberts, and D.H. Saxon, Z. Phys. **C39** (1988) 281.

[57] A. Cooper–Sarkar, R. Devenish and M. Lancaster, in: Proc. of 1991 HERA Physics Workshop, eds. W. Buchmüller and G. Ingelman, (DESY, Hamburg, 1992), Vol. **1**, p. 155.

[58] D.W. Duke, J.D. Kimel, and G.A. Sowell, Phys. Rev. **D25** (1982) 71;
S.N. Coulson and R.E. Ecclestone, Phys. Lett. **B115** (1982) 415; Nucl. Phys. **B211** (1983) 317;
A. Devoto, D.M. Duke, J.D. Kimel, and G.A. Sowell, Phys. Rev. **D30** (1984) 541;
J.L. Miramontes, J. Sanchez Guillén, and E. Zas, Phys. Rev. **D35** (1987) 863;
D.I. Kazakov et al., Phys. Rev. Lett. **65** (1990) 1535, Erratum: ibid. **65** (1990) 1921;
J. Sanchez Guillén et al., Nucl. Phys. **B353** (1991) 337.

[59] W.L. van Neerven and E.B. Zijlstra, Phys. Lett. **B272** (1991) 127;
E.B. Zijlstra and W.L. van Neerven, Phys. Lett. **B273** (1991) 476; Nucl. Phys. **B382** (1992) 11;
E.B. Zijlstra, PhD thesis, Leiden University, 1993.

[60] S.A. Larin and J.A.M. Vermaseren, Z. Phys. **C57** (1993) 93.

[61] J. Blümlein, DESY 93–095, J. Phys. **G**, in press.

[62] G. Barbagli and G. D'Agostini, in: Proc. of the HERA Workshop, Hamburg, October 1987, ed. R.D. Peccei, Vol. **1**, p. 135;
G. D'Agostini and D. Monaldi, Z. Phys. **C48** (1990) 467.

[63] R. van Woudenberg, F. Ould–Saada, F. Barreiro, J. del Peso, J.F. de Trocóniz, Y. Eisenberg, C. Glasman, U. Karshon, A. Montag, and S. Egli, in: Proc. of 1991 HERA Physics Workshop, eds. W. Buchmüller and G. Ingelman, (DESY, Hamburg, 1992), Vol. **2**, p. 770.

[64] K.J. Abraham, H. Jung, G. Schuler, and J. de Trocóniz, in: Proceedings of the 'ECFA Large Hadron Collider Workshop', Aachen 4–9 October 1990, eds. G Jarlskog and D. Rein, CERN 90–10, ECFA 90–133, Vol. **2** (CERN, Geneva, 1991), p. 899.

[65] W.L. van Neerven, in: Proc. of the Workshop 'Deep Inelastic Scattering', Teupitz, Brandenburg, April 1992, eds. J. Blümlein and T. Riemann, Nucl. Phys. B (Proc. Suppl.) **29A** (1992) 199.

[66] J. Smith and W.L. van Neerven, Nucl. Phys. **B374** (1992) 36;
E. Laenen, S. Riemersma, J. Smith, and W.L. van Neerven, Phys. Lett. **B291** (1992) 325; Nucl. Phys. **B392** (1993) 162, 229.

[67] L.N. Lipatov, Sov. J. Nucl. Phys. **23** (1976) 338; E.A. Kuraev, L.N. Lipatov, and V.S. Fadin, Sov. Phys. JETP **45** (1977) 199;
Y. Balitskii and L.N. Lipatov, Sov. J. Nucl. Phys. **28** (1978) 822.

[68] S. Catani, M. Ciafaloni, and F. Hautmann, Phys. Lett. **B242** (1990) 97; Nucl. Phys. **B366** (1991) 135; in: Proc. of 1991 HERA Physics Workshop, eds. W. Buchmüller and G. Ingelman, (DESY, Hamburg, 1992), Vol. **2**, p. 690; in: Proc. of the Workshop 'Deep Inelastic Scattering', Teupitz, Brandenburg, April 1992, eds. J. Blümlein and T. Riemann, Nucl. Phys. B (Proc. Suppl.) **29A** (1992) 182.

[69] E.L. Berger and D. Jones, Phys. Rev. **D23** (1981) 1521;
R. Baier and R. Rückl, Nucl. Phys. **B201** (1982) 1; **B218** (1983) 289;
J. Körner, J. Cleymans, M. Kuroda, and G. Gounaris, Phys. Lett. **B114** (1982) 195; Nucl. Phys. **B204** (1982) 6, Erratum: ibid. **B213** (1983) 546.

[70] A.D. Martin, C.K. Ng, and W.J. Stirling, Phys. Lett. **B191** (1987) 200;
S.M. Tkaczyk, W.J. Stirling, and D.H. Saxon, in: Proc. of the HERA Workshop, Hamburg, October 1987, ed. R.D. Peccei, Vol. **1**, p. 265.

[71] H. Jung, G. Schuler, and J. Terrón, in: Proc. of 1991 HERA Physics Workshop, eds. W. Buchmüller and G. Ingelman, (DESY, Hamburg, 1992), Vol. **2** p. 712 and Int. J. Mod. Phys. **A7** (1992) 7955.

[72] W.–Y. Keung and I.J. Muzinich, Phys. Rev. **D27** (1983) 1518;
H. Jung, D. Krücker, C. Greub, and D. Wyler, DESY 93–072.

[73] R. Barbieri, R. Gatto, and E. Remiddi, Phys. Lett. **B106** (1981) 497;
W. Kwong, P.B. Mackenzie, R. Rosenfeld, and J.L. Rosner, Phys. Rev. **D37** (1988) 3210.

[74] P.M. Zerwas et al., in preparation.

[75] V.N. Gribov and L.N. Lipatov, Sov. J. Nucl. Phys. **15** (1972) 438, 675;
G. Altarelli and G. Parisi, Nucl. Phys. **B126** (1977) 298;
Yu.L. Dokshitser, Sov. J. JETP **46** (1977) 641.

[76] A.J. Buras, Rev. Mod. Phys. **52** (1980) 199.

[77] D.J. Gross and F. Wilczek, Phys. Rev. Lett. **30** (1973) 1323; Phys. Rev. **D8** (1973) 3633; **D9** (1974) 980;
H.D. Politzer, Phys. Rev. Lett. **30** (1973) 1346; Phys. Rep. **14** (1974) 129;
H. Georgi and H.D. Politzer, Phys. Rev. **D9** (1974) 416.

[78] R. Wilson, Phys. Rev. **179** (1969) 1499;
N. Christ, B. Hasslacher, and A.H. Mueller, Phys. Rev. **D6** (1972) 3543.

[79] J. Blümlein, G. Ingelman, M. Klein, and R.Rückl, Z. Phys. **C45** (1990) 501.

[80] E.G. Floratos, D.A. Ross, and C.T. Sachrajda, Nucl. Phys. **B129** (1977) 66, Erratum: ibid. **B139** (1978) 545; Nucl. Phys. **B152** (1979) 417;
A. González–Arroyo, C. López, and F.J. Ynduráin, Nucl. Phys. **B153** (1979) 161;
A. González–Arroyo and C. López, Nucl. Phys. **B166** (1980) 429;
E.G. Floratos, P. Lacaze, and C. Kounnas, Phys. Lett. **B98** (1981) 89, 225;
G. Curci, W. Furmanski, and R. Petronzio, Nucl. Phys. **B175** (1980) 27;
W. Furmanski and R. Petronzio, Phys. Lett. **B97** (1980) 437;
C. López and F.J. Ynduráin, Nucl. Phys. **B183** (1981) 157.

[81] W. Caswell, Phys. Rev. Lett. **33** (1974) 244;
D.R.T. Jones, Nucl. Phys. **B75** (1974) 531.

[82] Wu–Ki Tung, Nucl. Phys. **B315** (1989) 378.

[83] J. Blümlein and M. Klein, Nuclear Instruments and Methods, **A329** (1993) 112.

[84] L. Baulieu and C. Kounnas, Nucl. Phys. **B155** (1979) 429.

[85] K. Prytz, Phys. Lett. **B311** (1993) 286.

[86] J. Blümlein, M. Klein, and T. Naumann, Proc. 'New Theories in Physics', Kazimierz, Poland 1988, ed. Z. Adjuk, World Scientific, Singapore, p. 228.

[87] S. Bethke, in: Proc. of the XXVI International Conference on High Energy Physics, Vol. I, August 6–12, 1992, Dallas, TX, ed. J.R. Sanford, (AIP, New York, 1993), p. 81.

[88] G. Altarelli, CERN–TH–6623–92, to appear in: *QCD – 20 Years Later*, Proc. of the International Workshop, Aachen, Germany, June 1992, eds. H.A. Kastrup and P.M. Zerwas, World Scientific, Singapore, 1993.

[89] T. DeGrand, Nucl. Phys. **B151** (1979) 485.

[90] J.P. Ralston and D.W. McKay, in: 'Physics Simulations at High Energies', ed. V. Barger, (World Scientific, Sigapore, 1987); Proc. of the Workshop 'Small–x Behaviour of Deep Inelastic Structure Functions in QCD', Hamburg, May 1990, eds. A. Ali and J. Bartels, Nucl. Phys. **B**, (Proc. Suppl.) **18C**, (1991) p. 86.

[91] L. Gribov, E. Levin and M. Ryskin, Nucl. Phys. **B188** (1981) 555; Phys. Rep. **100** (1983) 1.

[92] A.H. Mueller and Qiu, Nucl. Phys. **B286** (1985) 427.

[93] J. Bartels, J. Blümlein and G.A. Schuler, Z. Phys. **C50** (1991) 91.

[94] J. Collins and J. Kwiecinski, Nucl. Phys. **B335** (1990) 89;
M. Altmann, M. Glück, and E. Reya, Phys. Lett. **B285** (1992) 359.

[95] J. Bartels, A. DeRoeck and M. Loewe, Z. Phys. **C54** (1992) 635;
Wai–Keung Tang, Phys. Lett. **B278** (1992) 363;
J. Kwiecinski, A.D. Martin and P.J. Sutton, Phys. Lett. **B287** (1992) 254.

[96] J. Bartels, DESY 91–074; Proc. of the Workshop on 'Deep Inelastic Scattering', Teupitz, April 1992, Nucl. Phys. Suppl. Proc. **29A**, eds. J. Blümlein and T. Riemann, (North Holland, Amsterdam, 1992), p. 44; Phys. Lett. **B298** (1993) 204; DESY 93–028;
E. Levin, M. Ryskin, and A.G. Shuvaev, Nucl. Phys. **B387** (1992) 589;
J. Bartels and M.G. Ryskin, DESY 93–081.

[97] G. Marchesini, in: 'QCD at 200 TeV', eds. L. Cifarelli and Y. Dokshitser, (Plenum, New York, 1992), p. 183.

[98] I. Abt et al., H1 collaboration, DESY 93–117, August 1993.

[99] M. Derrick et al., ZEUS collaboration, DESY 93–110, August 1993.

[100] T. Ahmed et al., H1 collaboration, Phys. Lett. **B298** (1993) 469;
M. Derrick et al., ZEUS collaboration, Phys. Lett. **B303** (1993) 183.

[101] P. Amaudruz et al., NMC collaboration, Phys. Lett. **B295** (1992) 159 and Erratum to CERN–PPE/92–124, CERN, April 1993.

[102] A.C. Benvenuti et al., BCDMS collaboration, Phys. Lett. **B223** (1989) 485.